nature physics

Letter

https://doi.org/10.1038/s41567-022-01836-0

Autonomous waves and global motion modes in living active solids

Received: 20 April 2022

Accepted: 13 October 2022

Published online: 28 November 2022

Check for updates

Haoran Xu [1], Yulu Huang [2], Rui Zhang [2] & Yilin Wu [1]

Elastic active matter—also called an active solid—consists of self-propelled units embedded in an elastic matrix and it resists deformation. This shape-preserving property and the intrinsic non-equilibrium nature make active solids an attractive potential component for self-driven devices, but their mechanical properties and emergent behaviour remain poorly understood. Here, using a biofilm-based living active solid, we observe self-sustained elastic waves with wave properties not seen in passive solids, such as power-law scaling of wave speed with activity. Under isotropic confinement, the active solid develops two topologically distinct global motion modes that can be selectively excited, with a step-like frequency jump at the transition between the two modes. Our findings reveal spatiotemporal order in elastic active matter and may guide the development of solid-state adaptive or living materials.

Active matter consists of living or synthetic units that can convert local free energy input to mechanical work[1]. As an intrinsically non-equilibrium state of matter, active matter displays rich emergent behaviour such as dynamical collective motion[2–4] and self-organization[5–12]; it holds great potential for understanding the physics of living matter[1] and for the design of autonomous or self-driven materials with life-like properties[13,14]. Understanding the mechanical functionality of active matter as a continuum (that is, the ability to generate forces or extract work at length scales much larger than the individual unit) is an essential step to bridge the gap between practical applications and a myriad of fundamental science knowledge in the field learned over the past two decades[15]. However, such understanding has been limited, in part owing to the poor scalability of most experimental systems. Here we use millimetre-sized bacterial biofilms[16,17] to explore the emergent mechanical behaviour of elastic active matter or active solids[18–22]. We discover that mass elements in bacterial active solids are self-driven into local oscillatory motion. Under two-dimensional (2D) isotropic confinement, the local oscillation self-organizes into a pair of topologically distinct global motion modes. The mode selection is tunable by varying the activity of the active units; surprisingly, the two modes transit between each other with a sharp, step-like frequency jump at a certain activity threshold. Under anisotropic confinement with a major axis of symmetry, the local oscillation of mass elements is organized in space as self-sustained elastic standing waves. These results are observed in both experiments and numerical modelling with remarkable agreement. Furthermore, our model predicts that the phase of local oscillations is arranged as travelling waves in unconfined space, with the wave speed scaling as the -1/2 power of activity and the wavelength independent of activity. This property of active matter elastic waves is in stark contrast to the counterpart in passive mechanical waves where the wave speed does not depend on the driving amplitude of external stimuli. Our findings reveal unique mechanical properties of active matter and pave the way for investigating the non-equilibrium physics of elastic active matter in continuum. The findings may guide the development of solid-state adaptive or living materials, such as autonomous actuators for soft robotics[23,24], programmable tissues[25,26] and synthetic microbial consortia[27,28] with mechanical functionalities.

Elastic active matter consists of force-generating units embedded in an elastic matrix and they resist deformation like passive elastic solids; the shape-preserving property makes active solids a superior component for self-driven devices. Owing to the non-equilibrium nature, active solids are predicted to have novel mechanical properties that are not permitted in passive solids[20–22]. However, active solids have been investigated only in macroscopic analogue models using robotic structures[29–34], and an experimental system appropriate for the study of active solids as continuous media is lacking. Motile bacteria are premier experimental systems for active matter studies[1]. We envisaged that motile bacteria embedded in elastic polymer matrices may

[1]Department of Physics and Shenzhen Research Institute, The Chinese University of Hong Kong, Hong Kong, P. R. China. [2]Department of Physics, The Hong Kong University of Science and Technology, Hong Kong, P. R. China. e-mail: ylwu@cuhk.edu.hk

constitute a continuum body of active solid because of the superior scalability, so we turned to bacterial biofilms that consist of densely packed bacterial cells (>10^{11} cells per ml) encased by cell-derived extracellular polymers[16,17]. After testing several commonly used bacterial species, we identified early-stage *Proteus mirabilis* biofilms[35] as a prospective active solid. Cells extracted from such early-stage *P. mirabilis* biofilms (~0.8 μm in width and ~2 μm in length) typically retained motility instead of having transitioned into a sessile state, while there was prominent production of extracellular amyloid fibrils matrix (Extended Data Fig. 1 and Methods). In the *P. mirabilis* biofilm, cells are self-propelled by rotating flagellar filaments (~20 nm in diameter and ~5–10 μm in length) appended on cell surfaces, and flagellar rotation is fuelled by protonmotive force[36]. The overall storage modulus (that is, a measure of the elasticity of cell-matrix assembly) of the homogenized early-stage *P. mirabilis* biofilms is higher than the overall loss modulus and ranges from ~10^2 Pa to ~10^3 Pa (Extended Data Fig. 2 and Methods); thus, the early-stage *P. mirabilis* biofilms represent a viscoelastic solid[37] soft enough to be compliant with the active stress generated by bacteria (~1 Pa for a cell with single flagellum that generates a propulsive force of ~0.57 pN (ref. [38]) and acts on an area equivalent to the cross-sectional area of the cell body).

We fabricated early-stage *P. mirabilis* biofilms and measured the motion of mass elements in the system (Methods). The biofilms are quasi-2D and disk-shaped, with the top surface exposed to air and the bottom surface in contact with agar that provides nutrients and substrate adhesion. The system is laterally confined by a rim of immotile cells that express little extracellular polymer matrix (Methods and Extended Data Fig. 1a,b). A small fraction of cells embedded in the extracellular polymer matrix of the biofilm were labelled by genetically encoded fluorescent protein and were used as tracers of local mass elements (Methods). Strikingly, we found that mass elements in the biofilms are self-driven into local oscillatory motion with nearly homogeneous frequency across space (Fig. 1a,b and Extended Data Fig. 3). In circular disk-shaped biofilms of ~1 mm in diameter (Extended Data Fig. 1a; representing quasi-2D isotropic lateral confinement), the local oscillation of mass elements self-organizes into a pair of topologically distinct, self-driven global motion modes. In one mode, all mass elements being tracked in the biofilm followed a periodic quasi-circular trajectory in a synchronized manner (Fig. 1a, Supplementary Videos 1 and 2, and Methods); hence, the entire system underwent periodic translational motion and we referred to this mode as oscillatory translation. In the other mode, the mass elements followed periodic, synchronized quasi-linear trajectories that can be approximated as concentric circular arcs around the centre of the disk (Fig. 1b and Supplementary Videos 3 and 4); hence, the entire system underwent global rotation with periodically switching chirality and this mode is referred to as oscillatory rotation. These results confirmed that the mass elements in the biofilms were confined to orbiting about a fixed equilibrium position, as expected in elastic solids; thus, we call the early-stage *P. mirabilis* biofilms a bacterial active solid. Although *P. mirabilis* biofilm is our choice of study, we note that the solid-like global motion can also be found in *Serratia marcescens* (both oscillatory translation and rotation modes) and in *Escherichia coli* (oscillatory rotation mode), suggesting the generality of the findings (see Methods for details). Interestingly, active-solid-like behaviour similar to the oscillatory translation mode reported here has been found in macroscopic robotic structures[33], whose boundary conditions may prevent the development of global rotational motion.

The two distinct global motion modes found in the bacterial active solid under isotropic lateral confinement were also evident from the temporal dynamics of spatially averaged collective velocity measured by an optical flow technique (Fig. 1c–f, Supplementary Videos 5 and 6, and Methods). In the oscillatory translation mode, the two orthogonal components of spatially averaged collective velocity decomposed in Cartesian coordinates oscillate periodically with π/2 (clockwise) or 3π/2 (anticlockwise) phase shift (Fig. 1e). Statistically, the chirality of oscillatory translational motion appears unbiased (clockwise, 29 out of 60; anticlockwise, 31 out of 60), which is indicative of spontaneous chiral symmetry breaking. In contrast, in the oscillatory rotation mode, the tangential component of spatially averaged collective velocity decomposed in polar coordinates oscillates periodically, while the radial component is negligible (Fig. 1f). Interestingly, we found that the two emergent global motion modes in the bacterial active solid had a conspicuous difference in oscillation frequency (Methods), with the frequency in oscillatory translation mode (0.11 ± 0.04 Hz; mean ± s.d., $N = 60$) being about twofold of that in the oscillatory rotation mode (0.06 ± 0.02 Hz; mean ± s.d., $N = 41$). This finding will be further discussed below.

Under anisotropic lateral spatial confinement with a major axis of symmetry (such as oval-shaped geometry; Extended Data Fig. 1d and Methods), we discovered that the local oscillation of mass elements in bacterial active solids is organized in space with a unique pattern of phase distribution. The collective velocity component perpendicular to the major axis (denoted as the transverse component or v_y) resembles a standing wave: the phase distribution in space is discretized into regularly separated domains, with each domain having similar phases (Fig. 2a,b, Supplementary Video 7 and Methods); meanwhile, the instantaneous magnitude of v_y varies in space as a sinusoidal function (Fig. 2c). These features are also evident in the spatiotemporal autocorrelation of v_y along the major axis, which shows a characteristic pattern of a standing wave consisting of periodic, segmented domains with high correlation (Fig. 2d). By contrast, the phase of the collective velocity component parallel to the major axis (denoted as the parallel component or v_x) does not vary in space (Fig. 2a,b); the spatiotemporal autocorrelation of v_x along the major axis shows a pattern of periodic, horizontal lanes with high correlation (Fig. 2e). Taken together, the local oscillation of mass elements in such bacterial active solids under anisotropic lateral confinement is organized in space as a self-sustained transverse standing wave. We note that the phase of v_x always differs from that of v_y by π/2 or −π/2; thus, every mass element undergoes oscillatory elliptical motion.

To further understand the findings, we controlled the activity of mass elements in the bacterial active solid by tuning the speed of cells with violet-light illumination[39] (Extended Data Fig. 4, Supplementary Video 8 and Methods). For bacterial active solids under disk-like isotropic lateral confinement, we found that the oscillatory translation and rotation mode dominates at higher and lower activity, respectively. Surprisingly, the modes transit to each other abruptly at certain activity threshold (Fig. 3a,b) with a sharp, step-like frequency jump (a fold change of 2.04 ± 0.42; mean ± s.d., $N = 8$) at mode transition (Fig. 3c), which agrees with the approximately twofold frequency difference of the two global motion modes that naturally emerged in disk-shaped bacterial active solids. These results show that activity selectively excites the two global motion modes, revealing a unique emergent mechanical property of active solids. Interestingly, the oscillation frequency of both modes is positively correlated with activity (Fig. 3c). Such activity dependence of the oscillation frequency is also evident in the self-sustained standing waves in bacterial active solids under anisotropic lateral spatial confinement, where the frequency of standing waves increases with activity in a continuous manner (Fig. 3d) rather than taking discrete values as in passive elastic plates. The activity dependence of the oscillation frequency is another unusual mechanical property of active solids.

To rationalize our experimental results, we performed numerical modelling of active solids. We modified the boundary conditions of a particle-based model to describe active solids[18,40,41] by considering a collective of overdamped self-propelled particles connected by Hookean springs (with spring constant k_b) and initially arranged in a 2D triangular lattice (Extended Data Fig. 5a). Each particle represents a mass element consisting of ~1,000 cells (Methods) and has an intrinsic self-propulsion

https://doi.org/10.1038/s41567-022-01836-0

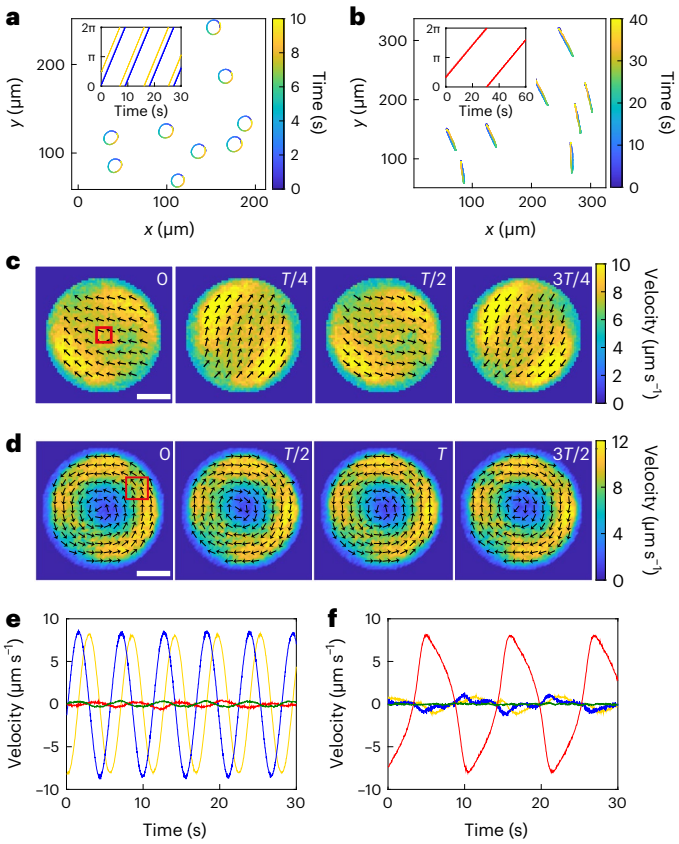

Fig. 1 | Emergent global motion modes in bacterial active solids derived from early-stage *P. mirabilis* biofilms under isotropic lateral confinement. **a**,**b**, Representative trajectories of mass elements in circular disk-shaped *P. mirabilis* biofilms that underwent global oscillatory translation (**a**) and oscillatory rotation (**b**). The trajectories in each panel were obtained by tracking embedded fluorescent cells in a representative experiment (>5 replicates; Methods). In **b**, the centre of rotation is located to the lower-left direction of the tracking domain. The colour map indicates time (unit, s). Inset in **a**: the position of a mass element was decomposed in Cartesian coordinates as (x, y) and the oscillation phases of the two components (with -π/2 phase difference; Methods) were plotted against time (yellow, x; blue, y); the phase plots of all mass elements being tracked ($N \geq 20$) are shown in an overlaid manner (the plots showed no dispersion because the phases were highly synchronized). Inset in **b**: the position of mass elements was decomposed in polar coordinates and the oscillation phases of the tangential components (Methods) were plotted against time in an overlaid manner ($N \geq 20$). **c**,**d**, Time sequences of collective velocity field in the global oscillatory translation mode (**c**; period $T = 5.6$ s) and oscillatory rotation mode (**d**; $T = 11.0$ s). The collective velocity field was measured by optical flow analysis based on phase-contrast images (Methods). The arrows represent the velocity direction and the colour map indicates the velocity magnitude. Unit of velocity, μm s^{-1}. Scale bar, 500 μm. Also see Supplementary Videos 5 and 6. The square box in the $T = 0$ s frame of **c** and **d** indicates the location of the field of **a** and **b**, respectively. **e**,**f**, Temporal dynamics of spatially averaged collective velocity (Methods) in the global oscillatory translation mode (**e**) and oscillatory rotation mode (**f**). The spatially averaged collective velocity was decomposed as Cartesian components (yellow and blue traces) and polar-coordinate components (red, tangential or azimuthal component; green, radial component). In the oscillatory translation mode, the polar-coordinate components are negligible; in the oscillatory rotation mode, both the radial and the Cartesian components are negligible. Panels **c** and **e**–**f** are based on data from the same experiments.

polarity, which accommodates the emergent self-propelled motion of the mass element driven by the propulsive forces of motile cells embedded in the mass element (Methods). Owing to substrate adhesion, the particles experience an elastic restoring force pointing towards their initial equilibrium positions, and particles initially sitting at the edge experience an additional elastic force pointing radially towards the edge to account for the steric effect of the lateral confinement boundary (Methods and Extended Data Fig. 5a). The position $\mathbf{x}_i$ and the self-propulsion polarity $\mathbf{n}_i$ of the ith particle evolve according to the following governing equations (Methods):

$$\dot{\mathbf{x}}_i = v_0 \mathbf{n}_i + \Xi_i(\mathbf{F}_i + D_r \hat{\xi}_r), \tag{1}$$

$$\dot{\mathbf{n}}_i = \beta[(\mathbf{F}_i + D_r \hat{\xi}_r) \cdot \hat{n}_i^{\perp}]\hat{n}_i^{\perp} + D_\theta \hat{\xi}_\theta - \Gamma \frac{\delta F_n}{\delta \mathbf{n}_i}, \tag{2}$$

where v_0 is the activity of particles and the direction of polarity $\mathbf{n}_i$ coincides with the direction of particles' self-propelled motion; Ξ_i is a translational mobility tensor; $\mathbf{F}_i$ is the total external elastic force acting on the particle controlled primarily by the local elasticity of the system (corresponding to spring constants as described in the caption of Extended Data Fig. 5a); $\hat{\xi}_r$ and $\hat{\xi}_\theta$ are randomly oriented unit vectors; $\hat{n}_i^{\perp}$ is a unit vector orthogonal to $\mathbf{n}_i$; D_r, D_θ, β and Γ are constants. The polarity $\mathbf{n}_i$ dynamics is controlled by three terms in equation (2), including a force-induced reorientation[18], a noise term and a term involving a Landau-type free energy $F_n = A(-2\mathbf{n}_i \cdot \mathbf{n}_i + (\mathbf{n}_i \cdot \mathbf{n}_i)^2 + \frac{1}{2}\kappa(\nabla \mathbf{n}_i)^2)$ (A and κ are constants)[42] that penalizes the deviation of $\mathbf{n}_i$ from being a unit vector (Methods). The gradient part $\frac{1}{2}\kappa(\nabla \mathbf{n}_i)^2$ in F_n allows for extending our model to active solids with microscopic geometrical anisotropy and orientational elasticity[20]; nonetheless, here we focused on active solids with isotropic elasticity by setting $\kappa = 0$ in F_n. Details of the model are described in Methods.

We found that all active particles in the modelled active solid are self-driven into local oscillatory motion with homogeneous frequency across space. Under 2D isotropic lateral confinement, our simulations successfully reproduced the two topologically distinct global motion modes observed in circular disk-shaped bacterial active solids (Extended Data Fig. 5, and Supplementary Videos 9 and 10). We scanned over the parameter space and obtained a phase map for the two global motion modes (Fig. 4a). We found that the emergence of the two global motion modes can be selected not only by the particle activity as demonstrated in the experiment but also by the system's local elasticity; moreover, there was a sharp, step-like frequency jump (approximately twofold change) at the phase boundary (Fig. 4b,c and Extended Data Fig. 6a), in agreement with the experimental result during activity-controlled mode transition shown in Fig. 3c. Informed by the simulation results, we examined the elasticity dependence of the global motion modes in experiment by controlling the temperature of bacterial active solids that scales linearly with the elasticity of polymer networks[43]. Indeed, we observed a transition between the two global motion modes at a certain temperature threshold accompanied by a sharp, approximately twofold frequency change (frequency ratio 2.04 ± 0.77; mean ± s.d., $N = 4$) (Extended Data Fig. 6b–d). A simulation-informed theoretical analysis provides quantitative insights into the frequency relations uncovered in the two emergent modes; see Supplementary Text for details. Essentially, denoting the frequency in the oscillatory translation and rotation mode as f_t and f_r, respectively, the theory yields $f_{t,r}$ being positively correlated with activity ($f_{t,r} \approx \sqrt{v_0}$) and the ratio f_t/f_r independent of activity v_0, which are in qualitative agreement with experimental and simulation results.

Under generic anisotropic lateral spatial confinement with a major axis of symmetry (such as in elliptical or rectangular geometry; Extended Data Fig. 7a), our simulations also successfully reproduced the self-sustained transverse standing waves found in experiments with bacterial active solids under anisotropic lateral confinement (Fig. 4d, Extended Data Fig. 7 and Supplementary Video 11). The remarkable agreement between experimental and simulation results prompted us to use the active solid model to explore the wave phenomena of active

https://doi.org/10.1038/s41567-022-01836-0

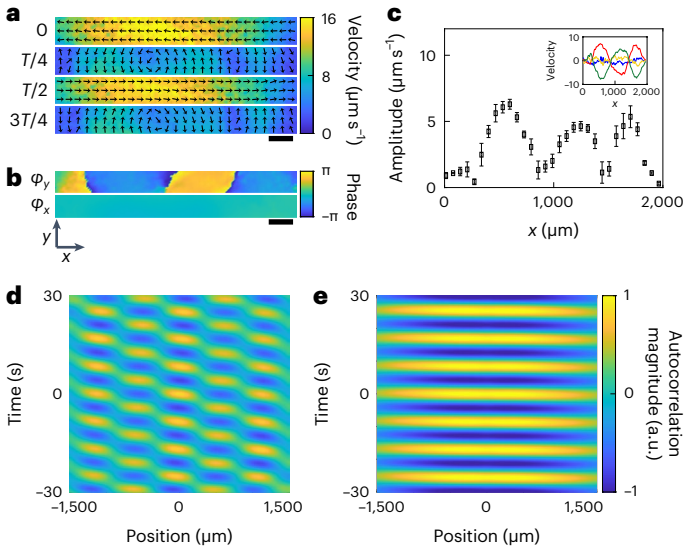

Fig. 2 | Self-sustained transverse standing waves in bacterial active solids under anisotropic lateral confinement. a, Time sequence of collective velocity field in an oval-shaped bacterial active solid (Extended Data Fig. 1d) that shows the transverse standing wave (with period $T = 8.6$ s) (Methods). The longer side of the rectangular domain shown here is parallel to the major axis of the bacterial active solid. The arrows represent the velocity direction and the colour map indicates the velocity magnitude. Unit of velocity, μm s^{-1}. Also see Supplementary Video 7. **b**, Spatial distribution of the oscillation phase of orthogonal collective velocity components associated with **a**. The phase of the parallel (v_x) and the transverse (v_y) collective velocity components are denoted as φ_x (top) and φ_y (bottom), respectively. The positive x axis in the specified coordinate system is parallel to the major axis of the active solid. Scale bars in **a** and **b**, 200 μm. **c**, Amplitude distribution of v_y along the major axis of the bacterial active solid. Data are presented as mean values (averaged over a time >60 s) ± s.d. Inset: temporal evolution of v_y profile along the major axis, with colours representing the time associated with **a** (blue, 0; red, $T/4$; yellow, $T/2$; green, $3T/4$). **d**,**e**, Spatiotemporal autocorrelation of v_y (**d**) and v_x (**e**) along the major axis of the bacterial active solid (Methods). The colour map to the right of **e** indicates the autocorrelation magnitude (a.u.). The data in this figure are from a representative experiment (>10 replicates).

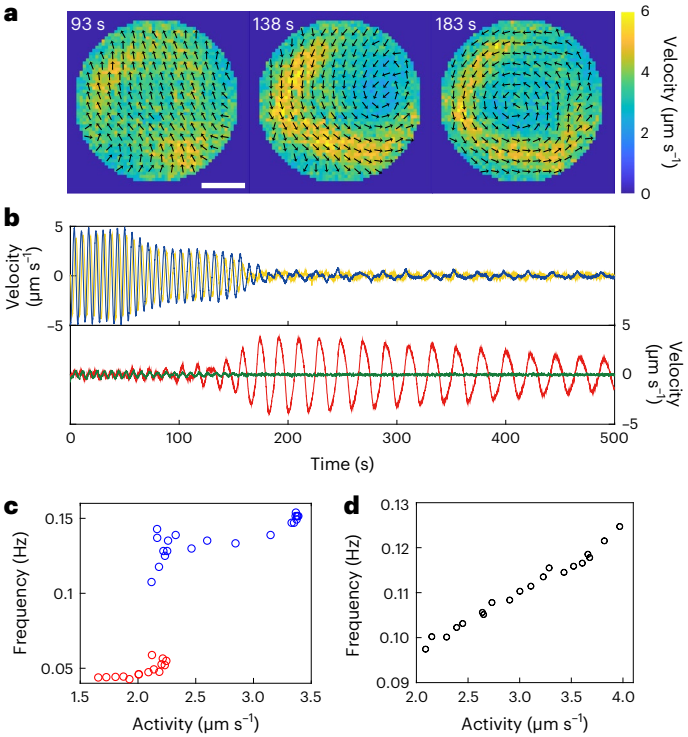

Fig. 3 | Activity selectively excites the global motion modes and controls frequency in bacterial active solids. a,**b**, Transition of global motion modes controlled by bacterial motility. A circular disk-shaped bacterial active solid was continuously illuminated by 406 nm violet light starting from $T \approx 60$ s (Methods). As the cell speed was decreased by violet light (Extended Data Fig. 4 and Methods), the bacterial active solid underwent mode transition. **a**, Snapshots of collective velocity field in the bacterial active solid during the transition from global oscillatory translation (for example, $T = 93$ s) to global oscillatory rotation (for example, $T = 183$ s). The collective velocity field was measured and plotted in the same manner as in Fig. 1c,d. Scale bar, 500 μm. **b**, Temporal dynamics of spatially averaged collective velocity of the bacterial active solid (Methods) during transition from the oscillatory translation mode to the oscillatory rotation mode following the decrease of bacterial motility. The spatially averaged collective velocity was decomposed as Cartesian components (yellow and blue traces; top) and polar-coordinate components (red, tangential or azimuthal component, green, radial component; bottom). **c**, Activity dependence of oscillation frequency in the bacterial active solid during mode transition. The horizontal axis represents the average collective speed of the active solid (Methods). The colour of the data points indicates the mode of global motion (blue, oscillatory translation; red, oscillatory rotation). The data in **a**–**c** are from a representative experiment (>10 replicates). **d**, Activity dependence of oscillation frequency in bacterial active solids under anisotropic lateral confinement that display self-sustained transverse standing waves (data from a representative experiment; >10 replicates).

solids in unconfined 2D space, which is currently not attainable in experiments (Methods). We discover that individual particles followed oscillatory quasi-circular motion and the phase of the local oscillation is arranged as travelling waves (Fig. 4e and Supplementary Video 12). While the frequency f of this travelling wave scales with particle activity v_0 as $f \approx v_0^{0.48}$ (Fig. 4f), the wavelength is independent of particle activity (Fig. 4f); thus, the wave speed U is proportional to frequency and also scales with activity as $U \approx v_0^{0.48}$. This result is in stark contrast to the counterpart in passive mechanical waves where the wave speed does not depend on the driving amplitude of external stimuli. Notably, the wave speed of such self-generated elastic active matter waves is on the order of a few hundred micrometres per second estimated based on values measured in the standing wave of bacterial active solids (frequency ~0.1 Hz, wavelength ~1–2 mm), which is much smaller than the speed of acoustic waves in ordinary passive solids. Unlike mechanical waves in passive solids, the elastic waves we uncovered in bacterial active solids are self-generated by the activity of mass elements. Our results illustrate that the inherent active nature of mass elements can give rise to unique properties of active matter waves.

To conclude, we have discovered an array of mechanical behaviours of elastic active matter that are not permitted in passive solids, including the formation of self-sustained elastic waves with activity-dependent wave properties and the emergence of two topologically distinct global motion modes with activity-dependent mode selection. The activity dependence of these uncovered mechanical behaviours provides simple means to control the emergent mechanical properties of solid-state active matter. In addition, our experimental system, that is, bacterial active solids derived from biofilms, has superior scalability and the convenience of engineering molecule-level interactions using tools from synthetic biology[27,28]; we expect that bacterial active solids will serve as a valuable experimental platform to explore the non-equilibrium physics of active solids in continuum[20–22]. Expanding the framework of classical continuum mechanics[20–22], lessons learned from bacterial active solids may inspire the design of novel functionalities in adaptive or living materials for soft robotics and biotherapeutics[23,24,26–28].

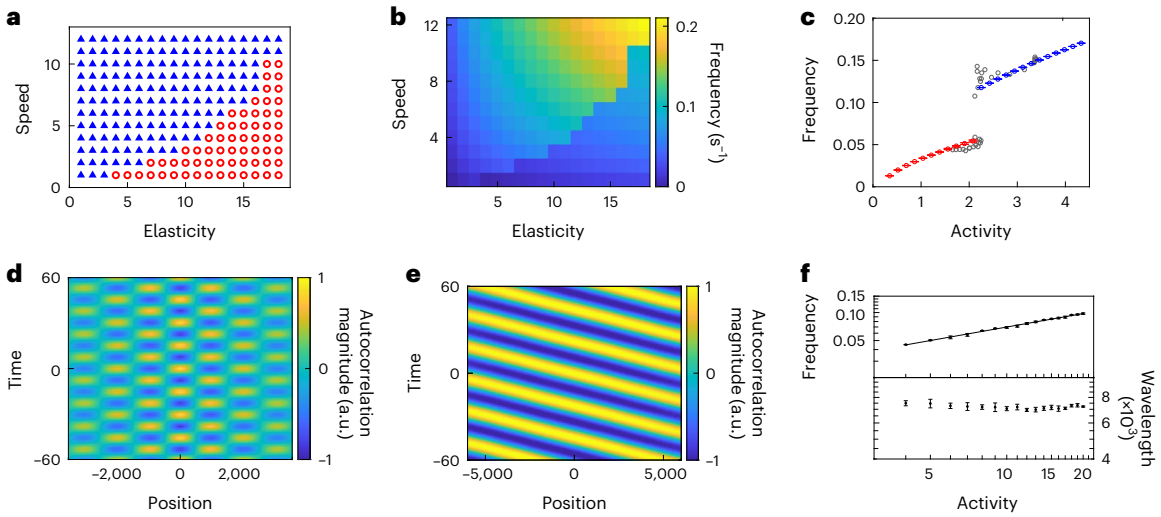

Fig. 4 | Global motion modes and self-sustained elastic waves in modelled active solids. a, Phase diagram of global motion modes in modelled active solids under isotropic lateral confinement. The phase diagram is plotted in the plane of particles' activity v_0 and system's local elasticity (with the interparticle spring constant k_b serving as a proxy; Methods). Triangles and circles represent oscillatory translation and rotation modes, respectively. Each data point in the phase diagram was obtained with 120 simulation runs (Methods). **b**, Distribution of oscillation frequency (indicated by the colour map) in the phase diagram of **a**. **c**, Oscillation frequency of the modelled active solid under isotropic lateral confinement as a function of v_0 (fixing $k_b = 14$). The colour of the data points indicates the mode of global motion (blue, oscillatory translation; red, oscillatory rotation). Data are presented as mean ± s.d. ($N = 100$ simulation runs). Empty circles overlaid to the plot are experimental data from Fig. 3c. **d**, Self-sustained transverse standing waves in a modelled active solid under elliptical lateral confinement. Similar to Fig. 2d, this panel shows the spatiotemporal autocorrelation of the transverse component of particle velocity along the major axis of the elliptical confinement (that is, the abscissa); the pattern of periodic, segmented domains with high correlation is characteristic of a standing wave. The colour map indicates the autocorrelation magnitude (a.u.). Also see Extended Data Fig. 7. **e**, Self-sustained travelling wave in a modelled active solid in unconfined 2D space. This panel shows the spatiotemporal autocorrelation of the transverse component of particle velocity along the wave propagation direction (that is, the abscissa); the pattern of periodic and tilted lanes with high correlation is characteristic of a travelling wave. The component of particle velocity parallel to the wave propagation direction shows the same autocorrelation pattern. The colour map indicates the autocorrelation magnitude (a.u.). **f**, Oscillation frequency (top) and wavelength (bottom) in unconfined 2D active solid as a function of particle activity v_0. The black line in the top panel is a linear fit to the log–log plot with a slope of 0.48 ± 0.01 ($R^2 = 0.997$). The data are presented as mean ± s.d. ($N = 100$ simulations runs).

Online content

Any methods, additional references, Nature Portfolio reporting summaries, source data, extended data, supplementary information, acknowledgements, peer review information; details of author contributions and competing interests; and statements of data and code availability are available at https://doi.org/10.1038/s41567-022-01836-0.

References

1. Marchetti, M. C. et al. Hydrodynamics of soft active matter. *Rev. Mod. Phys.* **85**, 1143–1189 (2013).
2. Vicsek, T. & Zafeiris, A. Collective motion. *Phys. Rep.* **517**, 71–140 (2012).
3. Bricard, A., Caussin, J.-B., Desreumaux, N., Dauchot, O. & Bartolo, D. Emergence of macroscopic directed motion in populations of motile colloids. *Nature* **503**, 95–98 (2013).
4. Wu, K.-T. et al. Transition from turbulent to coherent flows in confined three-dimensional active fluids. *Science* https://doi.org/10.1126/science.aal1979 (2017).
5. Sumino, Y. et al. Large-scale vortex lattice emerging from collectively moving microtubules. *Nature* **483**, 448–452 (2012).
6. Palacci, J., Sacanna, S., Steinberg, A. P., Pine, D. J. & Chaikin, P. M. Living crystals of light-activated colloidal surfers. *Science* **339**, 936–940 (2013).
7. Petroff, A. P., Wu, X.-L. & Libchaber, A. Fast-moving bacteria self-organize into active two-dimensional crystals of rotating cells. *Phys. Rev. Lett.* **114**, 158102 (2015).
8. Keber, F. C. et al. Topology and dynamics of active nematic vesicles. *Science* **345**, 1135–1139 (2014).
9. Wioland, H., Woodhouse, F. G., Dunkel, J. & Goldstein, R. E. Ferromagnetic and antiferromagnetic order in bacterial vortex lattices. *Nat. Phys.* **12**, 341–345 (2016).
10. Chen, C., Liu, S., Shi, X. Q., Chate, H. & Wu, Y. Weak synchronization and large-scale collective oscillation in dense bacterial suspensions. *Nature* **542**, 210–214 (2017).
11. Han, K. et al. Emergence of self-organized multivortex states in flocks of active rollers. *Proc. Natl Acad. Sci. USA* **117**, 9706–9711 (2020).
12. Liu, S., Shankar, S., Marchetti, M. C. & Wu, Y. Viscoelastic control of spatiotemporal order in bacterial active matter. *Nature* **590**, 80–84 (2021).
13. Needleman, D. & Dogic, Z. Active matter at the interface between materials science and cell biology. *Nat. Rev. Mater.* **2**, 17048 (2017).
14. Zhang, R., Mozaffari, A. & de Pablo, J. J. Autonomous materials systems from active liquid crystals. *Nat. Rev. Mater.* **6**, 437–453 (2021).
15. Gompper, G. et al. The 2020 motile active matter roadmap. *J. Phys. Condens. Matter* **32**, 193001 (2020).
16. Wilking, J. N., Angelini, T. E., Seminaraa, A., Brennera, M. P. & Weitz, D. A. Biofilms as complex fluids. *MRS Bull.* **36**, 385–391 (2011).
17. Wong, G. C. L. et al. Roadmap on emerging concepts in the physical biology of bacterial biofilms: from surface sensing to community formation. *Phys. Biol.* **18**, 051501 (2021).
18. Ferrante, E., Turgut, A. E., Dorigo, M. & Huepe, C. Elasticity-based mechanism for the collective motion of self-propelled particles with springlike interactions: a model system for natural and artificial swarms. *Phys. Rev. Lett.* **111**, 268302 (2013).

19. Hawkins, R. J. & Liverpool, T. B. Stress reorganization and response in active solids. *Phys. Rev. Lett.* **113**, 028102 (2014).
20. Maitra, A. & Ramaswamy, S. Oriented active solids. *Phys. Rev. Lett.* **123**, 238001 (2019).
21. Scheibner, C. et al. Odd elasticity. *Nat. Phys.* **16**, 475–480 (2020).
22. Scheibner, C., Irvine, W. T. M. & Vitelli, V. Non-Hermitian band topology and skin modes in active elastic media. *Phys. Rev. Lett.* **125**, 118001 (2020).
23. Rothemund, P. et al. A soft, bistable valve for autonomous control of soft actuators. *Sci. Robot.* **3**, eaar7986 (2018).
24. Preston, D. J. et al. Digital logic for soft devices. *Proc. Natl Acad. Sci. USA* **116**, 7750–7759 (2019).
25. Nitsan, I., Drori, S., Lewis, Y. E., Cohen, S. & Tzlil, S. Mechanical communication in cardiac cell synchronized beating. *Nat. Phys.* **12**, 472–477 (2016).
26. Park, S.-J. et al. Phototactic guidance of a tissue-engineered soft-robotic ray. *Science* **353**, 158–162 (2016).
27. Bittihn, P., Din, M. O., Tsimring, L. S. & Hasty, J. Rational engineering of synthetic microbial systems: from single cells to consortia. *Curr. Opin. Microbiol.* **45**, 92–99 (2018).
28. Duncker, K. E., Holmes, Z. A. & You, L. Engineered microbial consortia: strategies and applications. *Microb. Cell Fact.* **20**, 211 (2021).
29. Ferrante, E. et al. Self-organized flocking with a mobile robot swarm: a novel motion control method. *Adapt. Behav.* **20**, 460–477 (2012).
30. Shen, H., Tan, P. & Xu, L. Probing the role of mobility in the collective motion of nonequilibrium systems. *Phys. Rev. Lett.* **116**, 048302 (2016).
31. Chen, Y., Li, X., Scheibner, C., Vitelli, V. & Huang, G. Realization of active metamaterials with odd micropolar elasticity. *Nat. Commun.* **12**, 5935 (2021).
32. Zheng, E. et al. Self-oscillation and synchronisation transitions in elasto-active structures. Preprint at https://arxiv.org/abs/2106.05721 (2021).
33. Baconnier, P. et al. Selective and collective actuation in active solids. *Nat. Phys.* **18**, 1234–1239 (2022).
34. Zheng, Y., Huepe, C. & Han, Z. Experimental capabilities and limitations of a position-based control algorithm for swarm robotics. *Adapt. Behav.* **30**, 19–35 (2022).
35. Scavone, P. et al. Fimbriae have distinguishable roles in *Proteus mirabilis* biofilm formation. *Pathog. Dis.* https://doi.org/10.1093/femspd/ftw033 (2016).
36. Berg, H. C. Motile behavior of bacteria. *Phys. Today* **53**, 24–29 (2000).
37. Ferry, J. D. *Viscoelastic Properties of Polymers* (Wiley, 1980).
38. Chattopadhyay, S., Moldovan, R., Yeung, C. & Wu, X. L. Swimming efficiency of bacterium *Escherichia coli*. *Proc. Natl Acad. Sci. USA* **103**, 13712–13717 (2006).
39. Taylor, B. L. & Koshland, D. E. Intrinsic and extrinsic light responses of *Salmonella typhimurium* and *Escherichia coli*. *J. Bacteriol.* **123**, 557–569 (1975).
40. Ferrante, E., Turgut, A. E., Dorigo, M. & Huepe, C. Collective motion dynamics of active solids and active crystals. *New J. Phys.* **15**, 095011 (2013).
41. Woodhouse, F. G., Ronellenfitsch, H. & Dunkel, J. Autonomous actuation of zero modes in mechanical networks far from equilibrium. *Phys. Rev. Lett.* **121**, 178001 (2018).
42. Landau, L. & Lifshitz, E. *Statistical Physics* (Pergamon Press, Oxford, 1980).
43. De Gennes, P.-G. & Gennes, P.-G. *Scaling Concepts in Polymer Physics* (Cornell Univ. Press, 1979).

Methods

No statistical methods were used to predetermine sample size.

Bacterial strains

The following strains were used: wild-type *P. mirabilis* BB2000 and a fluorescent *P. mirabilis* KAG108 (BB2000 background with constitutive expression of green fluorescent protein (GFP)[44], from Karine Gibbs, Harvard University, Cambridge, MA); *S. marcescens* ATCC 274 and its derivative strains from Rasika Harshey, University of Texas at Austin; *E. coli* HCB1 (from Howard Berg, Harvard University, Cambridge, MA) and its derivative strains. Single-colony isolates were grown overnight (~13–14 h) with shaking in LB medium (1% Bacto Tryptone, 0.5% yeast extract, 0.5% NaCl) at 30 °C to stationary phase. For *P. mirabilis* KAG108, ampicillin (100 μg ml^{-1}) was added to the growth medium to maintain the plasmid.

Agar plates

LB agar (Difco Bacto agar at specified concentrations infused with 1% Bacto Tryptone, 0.5% yeast extract, 0.5% NaCl) was autoclaved and stored at room temperature. Before use, the agar was melted in a microwave oven, cooled to ~60 °C, and pipetted in 10 ml aliquots into 90 mm polystyrene Petri plates. The plates were swirled gently to ensure surface flatness, and then cooled for 10 min without a lid inside a large Plexiglas box before inoculation of bacterial culture. To visualize the amyloid fibrils in *P. mirabilis* biofilms, the LB agar plates were supplemented with the fluorescence dye thioflavin T (Sigma; catalogue number T3516-5G; at a final concentration of 10 μM) and the plates were prepared under the same conditions as specified above. Thioflavin T is commonly used to stain biofilm matrix consisting of amyloid fibrils[45]. The presence of thioflavin T does not affect the experimental phenomena reported in this study.

Fabrication of bacterial active solid

To fabricate the bacterial active solid derived from *P. mirabilis* biofilms, overnight *P. mirabilis* cultures were inoculated onto a 0.6% LB agar plate (as described above). To track the motion of mass elements by following the trajectory of single cells embedded in *P. mirabilis* biofilms, overnight culture of the GFP-tagged *P. mirabilis* KAG108 was mixed with wild-type *P. mirabilis* at 0.05% before inoculating the agar plates. The inoculated plates were dried for 10 min without a lid inside the Plexiglas box. The plates were then covered and incubated at 37 °C and ~95% relative humidity in an incubator with a water tray for ~14 h. Circular *P. mirabilis* colonies incubated for this duration of time reached a diameter of 1,650 ± 270 μm (mean ± s.d., $N = 102$) and were at the early stage of biofilm development, with cells therein typically being motile and with prominent production of extracellular amyloid fibrils matrix in the inner region. The height at the centre of the colonies was ~25 μm, and it decreased to ~10 μm over a radial distance of ~700 μm (corresponding to a slope of ~1.2°). The inner region of *P. mirabilis* colonies with extracellular matrix production (that is, the biofilm region) (Extended Data Fig. 1b) is where we choose to study and refer to as early-stage biofilm or bacterial active solid. As shown in single-cell tracking videos (Supplementary Videos 2 and 4), the orientations of cells embedded in the extracellular matrix appear to lack long-range order (nonetheless, a certain extent of local orientational ordering could not be excluded), and the cell orientations do not rotate during the global motion of the biofilm. The outer rim of *P. mirabilis* colonies is mostly occupied by immotile cells that have transitioned to the sessile state but expressed little extracellular matrix; the width of this outer immotile rim varies from tens to hundreds of micrometres. This immotile rim serves as the lateral spatial confinement for the bacterial active solid; the lateral confinement is expected to exert steric repulsion that restricts radial but not tangential movement of the mass elements near the edge of the bacterial active solid. Colonies that have developed from an isolated inoculum are circular and disk-shaped. When two inocula happen to be nearby, the colonies arising from these inocula will merge into one oval-shaped colony, with the ratio of the long and short axes controlled by the initial distance between the inocula. The circular and oval-shaped colonies provided the biofilms (or bacterial active solids) with isotropic lateral spatial confinement and anisotropic spatial confinement with a major axis of symmetry, respectively.

The onset of the reported active solid motion requires sufficient biofilm matrix expression. Well before the presence of biofilm matrix, the entire colony is liquid-like and cells move freely, displaying bacterial turbulence often seen in dense bacterial suspensions. Once emerged, the active solid motion may last for several hours. Typically, the oscillatory translation mode first appears, and the motion may transit to the oscillatory rotation mode as the expression level of extracellular amyloid fibre matrix further increases and/or the motility of cells decreases. As a colony continues to grow, its thickness increases and cells therein eventually lose motility after ~30 h of growth (most likely due to depletion of nutrients and oxygen within the thick colony); the biofilm then becomes motionless.

Active solid motion can also be found in *S. marcescens* and *E. coli* biofilms. In *S. marcescens* biofilms with an overall storage modulus of ~10–10^3 Pa (in the experimentally relevant range of strain 0–40%), we found both oscillatory rotation and translation modes (Extended Data Fig. 8 and Supplementary Video 13). Under the same growth conditions as *P. mirabilis* biofilms, the overall storage modulus of *E. coli* biofilms is ~10^3–10^5 Pa, but it can be lowered by growing *E. coli* biofilms in a more humid environment (for example, depositing ~5 ml LB broth around the edge of the Petri dish). In *E. coli* biofilms with an overall storage modulus of ~10^2–10^4 Pa, we found that the biofilms can display the oscillatory rotation mode but not the oscillatory translation mode. This result is consistent with the phase map (Fig. 4a), which predicts oscillatory rotation mode at a relatively high elasticity.

Microscopy imaging

All imaging was performed on a motorized inverted microscope (Nikon TI-E). To examine the expression of extracellular matrix, amyloid fibrils in *P. mirabilis* biofilms were visualized using a ×10 objective (Nikon CFI Achromat ×10, numerical aperture 0.25, working distance 7.0 mm) via a cyan fluorescence protein filter cube (excitation: 425/26 nm, emission: 479/40 nm, dichroic: 458 nm, FF458-Di02-25×36; Semrock), and images were recorded with a scientific complementary metal–oxide–semiconductor (sCMOS) camera (Andor Zyla 4.2 PLUS USB 3.0). To track the motion of mass elements in bacterial active solids derived from *P. mirabilis* biofilms, GFP-tagged *P. mirabilis* KAG108 cells embedded in the biofilm were imaged in epifluorescence using a ×20 objective (Nikon S Plan Fluor ×20, numerical aperture 0.45, working distance 8.2–6.9 mm) and an fluorescein isothiocyanate filter cube (excitation 482/35 nm, emission 536/40 nm, dichroic 506 nm; Semrock), with the excitation light provided by a mercury precentred fibre illuminator (Nikon Intensilight); meanwhile, to verify that the observed single-cell motion coincided with the motion of local mass elements where the cells were embedded, the background motion of *P. mirabilis* biofilm was imaged in phase contrast through the same optical system, with the illumination light provided by a white-light light-emitting diode (catalogue number MCWHL5; Thorlabs) installed above the microscope stage. Recordings were made with the sCMOS camera at 20 fps and at full frame size (2,048 × 2,048 pixels); fluorescent and phase-contrast images were recorded in alternate frames at 10 fps. The camera was controlled by NIS Elements (Nikon); the white-light light-emitting diode was switched on only during the acquisition of phase-contrast images and was triggered by 10 Hz Transistor-Transistor Logic signals sent from a custom-programmed Arduino microcontroller that modulated the 20 Hz fire output from the camera. To measure the collective velocity field in bacterial active solids, the sample was imaged in phase contrast with a ×4 (Nikon Plan Fluor ×4, numerical aperture 0.13, working distance 16.5 mm) objective. Recordings were made with the sCMOS

camera at 10 fps and at full frame size (2,048 × 2,048 pixels). To study the dynamics of the global motion modes and elastic waves in bacterial active solids at different activity level of mass elements, the speed of cells in the active solid was tuned by violet-light illumination[46] at 528 mW cm^{-2} provided by Nikon Intensilight and passing through the ×4 objective via a 406 nm filter (406/15 nm; FF01-406/15-25, Semrock); in the meantime, phase-contrast images of the active solid were recorded through the same ×4 objective by the sCMOS camera at 10 fps and at full frame size (2,048 × 2,048 pixels). In all experiments, the Petri dishes were covered with a lid to prevent evaporation and air convection. The sample temperature was maintained and controlled via a custom-built temperature-control system installed on the microscope stage.

Rheology of bacterial active solid

Rheological measurements of the bacterial active solid derived from *P. mirabilis* biofilms were performed in a rheometer (Anton Paar Physica MCR 301). The plate used for oscillatory shear measurements was CP50-1 (diameter 49.972 mm, angle 0.990° and 99 µm gap; Anton Paar, part number 79040 serial: 20173). The overall storage modulus (G') and loss modulus (G'') as a function of strain were measured in shear-strain-amplitude sweep mode (at constant frequency). The oscillation frequency and the temperature of the rheometer were set at 1 Hz and 37 °C, respectively. The temperature of the sample was controlled by the rheometer via a Peltier convection system connected to a water bath. A solvent trap equipped in the rheometer was used to reduce evaporation. Before rheology measurement, the *P. mirabilis* biofilms were gently scraped from Petri plates and collected into an Eppendorf tube, and the tube was heated at 55 °C for ~30 min to sterilize the bacterial cells without causing lysis. We note that this homogenization process might cause a certain disruptive effect to the biofilm structure, and thus the samples prepared for the rheological measurement should be taken as an approximation to the intact biofilms.

Image processing and data analysis for experiments

Images were processed using the open-source Fiji (ImageJ) software (http://fiji.sc/Fiji) and custom-written programs in MATLAB (MathWorks). To track the motion of local mass elements by following the trajectory of embedded single cells, trajectories of cells were obtained based on the recorded fluorescence videos, using a custom-written program in MATLAB published previously[47]. The cells' trajectories were then used to analyse their velocity and motion pattern. To compute the oscillation phase of individual cells embedded in circular disk-shaped bacterial active solids (insets of Fig. 1a,b), the position of individual cells extracted from their trajectories (lasting longer than 40 s) obtained by single-cell tracking was decomposed as Cartesian components (x, y) (for bacterial active solids undergoing oscillatory translation) or polar-coordinate components (r, θ) (for bacterial active solids undergoing oscillatory rotation; r denotes radial component and θ denotes tangential or azimuthal component, and the origin was chosen at the centre of the disk-shaped bacterial active solid). The position components $x(t)$, $y(t)$ and $\theta(t)$ were then fitted by sinusoidal functions using the least-squares method in MATLAB in the form of $A\sin(\omega t + \varphi_0)$, where A, ω and φ_0 are fitting parameters and $(\omega t + \varphi_0)$ was taken as the oscillation phase of individual cells.

To measure the collective velocity field of bacterial active solids, we first performed optical flow analysis based on phase-contrast time lapse videos using the built-in functions of MATLAB with a grid size of 1 pixel × 1 pixel. Before the optical flow analysis, the microscopy images were smoothed to reduce noise by convolution with a Gaussian kernel of standard deviation 1. The results were insensitive to different parameters of smoothing. To examine the uncertainty of the collective velocity measurement, we compared the collective velocity obtained by optical flow analysis and the average velocity of cells in the same field of view obtained by single-cell tracking in fluorescence images. We found that their difference was negligible (~4%). The excellent performance of optical flow velocimetry in our experimental system is due to the highly coherent motion of cells (that is, there is no relative motion between the cell bodies) when the system displays the active solid behaviour. The optical flow analysis yielded space- and time-dependent collective velocity field $\mathbf{v}(\mathbf{r}, t)$, or in Cartesian coordinates $(v_x(x, y, t), v_y(x, y, t))$. To compute the oscillation frequency, amplitude and phase of local mass elements in bacterial active solids, the obtained collective velocity field was coarse-grained by averaging over windows of a size 26 µm × 26 µm. The Cartesian components of coarse-grained collective velocity $\bar{v}_x(x, y, t)$and $\bar{v}_y(x, y, t)$at position (x, y) are fitted by sinusoidal functions using the least-squares method in MATLAB in the form of $A\sin(2\pi ft + \varphi_0)$, where A, f and φ_0 are fitting parameters that represent the velocity amplitude, frequency and phase shift of the local oscillation at position (x, y), respectively. The phase of the local oscillation at position (x, y) at time t is $(2\pi ft + \varphi_0)$. As the frequency of the local oscillation is nearly homogeneous in space for a given bacterial active solid (Extended Data Fig. 3), we took the spatial average of the fitted f as the oscillation frequency of the entire system being discussed. To characterize the self-sustained elastic waves in bacterial active solids, the spatiotemporal autocorrelation along certain direction (for example, the major axis of bacterial active solids under anisotropic lateral confinement denoted as x axis) for a collective velocity component (for example, $v_y(x, y, t)$ component perpendicular the major axis) was computed as $C(\Delta x, \Delta t) = \frac{<v_y(x,t)v_y(x+\Delta x,t+\Delta t)>_{x,t}}{<v_y(x,t)^2>_{x,t}}$, where angular brackets $\langle \ldots \rangle_{x,t}$ indicate averaging over the spatial coordinate on the chosen direction and time t.

To compute the spatially averaged collective velocity of bacterial active solids under isotropic lateral confinement, we decomposed the obtained collective velocity field $\mathbf{v}(\mathbf{r}, t)$ in Cartesian coordinates as $(v_x(x, y, t), v_y(x, y, t))$ and in polar coordinates as $(v_r(r, \phi, t), (v_\phi(r, \phi, t))$ (v_r denotes radial component and v_ϕ denotes tangential or azimuthal component; the origin of polar-coordinate system is chosen at the centre of the circular disk-shaped bacterial active solid). Each of these collective velocity components were then spatially averaged over the domain within two-thirds of the radius of the bacterial active solid (to exclude the near-boundary region with a larger slope of height variation), yielding the corresponding components of the spatially averaged collective velocity $(V_x(t), V_y(t))$ and $(V_r(t), V_\phi(t))$. The average collective speed of bacterial active solids (that is, activity in the horizontal axis of Fig. 3c,d) was computed as the root mean square of the magnitude of collective velocity vectors in the collective velocity field $\mathbf{v}(\mathbf{r}, t)$ averaged over several oscillation periods. A more accurate definition of cell activity is the self-propulsive force generated by flagellar motility of an average cell. However, we could not make direct measurement of the self-propulsive force and thus the speed of cells becomes an appropriate proxy.

To determine the specific mode of global motion in bacterial active solids under isotropic lateral confinement, we used the relative dominance of the Cartesian or polar-coordinate components of the spatially averaged collective velocity. Specifically, we fitted the spatially averaged collective velocity components $V_x(t)$, $V_y(t)$, $V_r(t)$, $V_\phi(t)$ obtained by procedures as described above into sinusoidal functions (using the least-squares method in MATLAB) in the form of $V(t) = B\sin(2\pi ft + \varphi_0)$, where B, f and φ_0 are fitting parameters that represent the collective velocity amplitude, oscillation frequency and phase shift, respectively. Note that f is equivalent to the spatial average of the frequency of local oscillations described above. The fitting yielded four sets of parameters $(B_i, f_i, \varphi_{0(i)})$ corresponding to the amplitude, oscillation frequency and phase shift, respectively, of each $V_i(t)$, with the index i being x, y, r, ϕ. In all experiments, we found that $B_r \approx 0$ and $f_x \approx f_y$. If $(B_x^2 + B_y^2)^{1/2} > 5B_t$, the global oscillatory motion of bacterial active solids was classified as oscillatory translation mode; if $B_\phi > 5(B_x^2 + B_y^2)^{1/2}$, the global oscillatory motion was classified as oscillatory rotation mode; for all other cases, the global oscillatory motion of bacterial active solids was

classified as coexistence mode. The coexistence mode was observed both in experiments (Extended Data Fig. 9) and in bead–spring model simulations near the mode transition thresholds at intermediate activity and elasticity (Extended Data Fig. 10). Interestingly, the frequencies of the two global motion modes in a mixed-mode state were always either almost identical ($f_t \approx f_r$; Extended Data Fig. 9a) or doubled ($f_t \approx 2f_r$; Extended Data Fig. 9b). In the first scenario ($f_t \approx f_r$), mass elements in the bacterial active solid followed quasi-elliptical trajectories (Extended Data Fig. 9c). By contrast, in the other scenario ($f_t \approx 2f_r$), mass elements followed figure-of-eight shaped curves (known as lemniscates) (Extended Data Fig. 9d). Presumably the mode coexistence represents an incomplete mode transition process, reminiscent of a phase-coexistence state during a first-order phase transition.

During the transition between the oscillatory translation mode and the oscillatory rotation mode in bacterial active solids under isotropic lateral confinement while continuously varying bacterial speed or temperature, the oscillation frequency varied with time. Instead of performing sinusoidal fits as described above, we computed the oscillation frequency of global motion at a specific time as the inverse of the time interval between the two adjacent peaks of an appropriate component of spatially averaged collective velocity (choosing one of the Cartesian components for the oscillatory translation mode and the tangential component in polar coordinates for the oscillatory rotation mode, respectively).

Simulation

To understand the dynamical phenomena uncovered in the bacterial active solid, we adopted a particle-based simulation framework[18,40,41] and considered a collective of overdamped self-propelled particles connected by springs. Each particle in the simulation represents a circular disk-shaped mass element of diameter ~16 μm and height ~20 μm; thus, a mass element consists of ~1,000 cells (~0.8 μm in width and ~2.0 μm in length), assuming a cell volume fraction of ~0.2 in the biofilm[48]. The particles were initially arranged in a 2D triangular lattice truncated by a circular domain with radius R. For the ith active particle or bead, its position $\mathbf{x}_i$ and self-propulsion polarity $\mathbf{n}_i$ evolve according to equations (1) and (2). In equation (1), the translational mobility tensor is given by $\Xi_i = \alpha_{||}\hat{n}_i\hat{n}_i + \alpha_{\perp}(I - \hat{n}_i\hat{n}_i)$, with $\hat{n}_i$ being the unit vector parallel to $\mathbf{n}_i$, $\alpha_{||}$ (or $\alpha_{\perp}$) being the parallel (or perpendicular) inverse translational damping coefficients, and I being a 2×2 identity matrix; in equation (2), β is the inverse rotational damping coefficient.

The particle's self-propulsion velocity (that is, $v_0\mathbf{n}_i$ in equation (1)) in our model represents the velocity of emergent self-propelled motion of a mass element, which presumably results from alignment of self-propulsive forces of motile cells within the mass element. Here the direction of polarity vector $\mathbf{n}_i$ of a particle or mass element can be regarded as the direction of statistically averaged self-propulsive forces of all cells in the mass element; the magnitude of $\mathbf{n}_i$ is variable and reflects the degree of alignment of cells' self-propulsive forces. Meanwhile, similar to the average collective speed in the horizontal axis of Fig. 3c,d, the particle activity v_0 should be interpreted as a proxy of the magnitude of self-propulsive force generated by flagellar motility of a typical cell in the mass element. The spontaneous alignment of self-propulsive forces of motile cells in a mass element is probably due to cell-matrix interactions within the mass element; at steady state, we expect that the self-propulsive forces tend to be well aligned to a common direction and thus the polarity $\mathbf{n}_i$ approaches a unit vector (or the particle's self-propulsion speed $|v_0\mathbf{n}_i|$ approaching v_0; note that this is different from the particle's apparent speed). In the model, this scenario is realized by the Landau-type free energy term F_n, which controls the magnitude of $\mathbf{n}_i$ and penalizes the deviation of $\mathbf{n}_i$ from being a unit vector.

As described in the main text and Extended Data Fig. 5a, three types of Hookean spring are involved in the model, namely an interparticle spring, a restoring spring and a boundary spring with spring constants k_b, k_s and k_r, respectively. The elastic interaction between mass elements mediated through the biofilm matrix is characterized by the springs with stiffness k_b; the springs with stiffness k_s account for the adhesion between the bacterial active solid and the substrate, which ensures that the centre of mass of the system is confined to orbiting about a fixed equilibrium position; the springs with stiffness k_r account for an effective steric effect of the lateral confinement boundary and maintain the in-plane geometrical shape of the bacterial active solid. Therefore, the external elastic force experienced by the ith particle $\mathbf{F}_i$ is a sum of three terms, $\mathbf{F}_i = \mathbf{F}_{b(i)} + \mathbf{F}_{s(i)} + \mathbf{F}_{r(i)}$, with each term given below.

The first term $\mathbf{F}_{b(i)}$ is a sum of elastic forces between the ith particle and its spring-connected neighbours (denoted as set S_i):

$$\mathbf{F}_{b(i)} = \sum_{j\in S_i} -k_b(|\mathbf{r}_{ij}| - l_0)\mathbf{r}_{ij}/|\mathbf{r}_{ij}|,$$

where l_0 is the equilibrium distance of interparticle springs with spring constant k_b, and $\mathbf{r}_{ij} = \mathbf{x}_i - \mathbf{x}_j$. The second term $\mathbf{F}_{s(i)} = -k_s(\mathbf{x}_i - \mathbf{x}_{0(i)})$ is a linear elastic restoring force that pulls the ith particle towards its equilibrium position $\mathbf{x}_{0(i)}$. The third term $\mathbf{F}_{r(i)}$ accounts for the steric effect of the lateral confinement boundary and thus it applies to particles initially sitting at the edge only; for instance, under circular lateral confinement, such particles are those with the position satisfying $||\mathbf{x}_{0(i)} - \mathbf{x}_{0(c)}| - R| < l_0$ where R is the radius of the circular lateral confinement and $\mathbf{x}_{0(c)}$ is the equilibrium position of the centre of the modelled active solid. $\mathbf{F}_{r(i)}$ is a linear elastic restoring force pointing towards the edge in parallel to the normal direction $\hat{\mathbf{n}}_{i,boundary}$ (that is, the unit vector perpendicular to the lateral confinement boundary) given by $\mathbf{F}_{r(i)} = -k_r[(\mathbf{x}_i - \mathbf{x}_{0(i)}) \cdot \mathbf{n}_{i,boundary}]\mathbf{n}_{i,boundary}$.

As active units in the bacterial active solid (each active unit consisting of an associated group of motile cells) are densely packed, an active unit would find it more difficult to move sideways than to move along its polarity direction due to steric hindrance. This indicates that $\alpha_{\perp} << \alpha_{||}$ for active particles in the model; for convenience we chose $\alpha_{\perp} = 0$. All simulations were carried out with $\alpha_{||} = 10$, $\beta = 1.2$, $D_r = 0.0001$, $D_\theta = 0.01$, $\Gamma = 1$, $A = 0.1$, $\kappa = 0$, initial or equilibrium interparticle distance $l_0 = d = 65$ and time step $\Delta t = 0.0005$. The emergence of the two global oscillation modes does not require the presence of noise (that is, setting both D_r and D_θ to zero does not affect the results); also the simulation results are robust as long as $D_r \leq 10^2$ (with the ratio between D_r and D_θ fixed).

To match with experimental results, we set one time unit as 1 s and one length unit as 0.25 μm. For simulations of active solids under isotropic lateral confinement, the radius of the circular simulation domain was chosen as $R = 15d$ with the particle number $N = 511$; for simulations with elliptical lateral confinement, the semi-major and semi-minor axis of the simulation domain were $a = 240d$ and $b = 9d$, respectively, with the particle number $N = 2{,}419$; for simulations in unconfined 2D space, the size of the simulation domain was $480d \times 480d$ with the particle number $N = 231{,}121$. Also, for simulations with either isotropic or anisotropic lateral spatial confinement, we kept the ratios between the interaction spring constants k_b, k_s and k_r as $k_r = k_b/20$ and $k_s = k_b/270$ unless otherwise specified; the values of k_s and k_r relative to k_b were selected to best fit the experimental results, including mode selection and approximately twofold frequency change during the transition. For simulations in unconfined 2D space, the boundary spring constant k_r (for the interaction between cells and the lateral confinement boundary) was set as 0, while the ratio between k_b and k_s was kept as $k_s = k_b/270$. All simulations began with a random orientational distribution of particle polarity. Despite the similarity between our model and the models developed in refs. [18,40], we did not observe the persistent translation and rotation predicted in these earlier studies. The difference is due to the different boundary conditions we used (including lateral spatial confinement and substrate adhesion).

We note that the spring constant k_b can be mapped to the shear modulus (storage modulus) G obtained via rheological measurement

in the experiment. Modelling the bulk part of the biofilm as a triangular elastic spring network, the relationship between Young's modulus E and bulk spring constant k_b can be written as $E = 2k_b/(\sqrt{3}H_e)$, where H_e is the height of the biofilm ($H_e \approx 20$ μm). Noting that $G = \frac{E}{2(1+\nu)}$ and assuming the Poisson's ratio of the biofilm $\nu \approx 0.5$, we have $k_b = \sqrt{3}EH_e/2 \approx 3\sqrt{3}GH_e$. As G is in the range of 10^2–10^3 Pa (Extended Data Fig. 2), we have $k_b \approx 10^3$–10^4 pN μm^{-1}. To convert the parameters in physical units to dimensionless ones for simulations, we choose one length unit as $\bar{\xi} = 0.25$ μm, one velocity unit as $\bar{v} = 0.25$ μm s^{-1}, and one unit of spring stiffness as $\bar{k} = 1{,}000$ pN μm^{-1}. With these basic units, the typical value of k_b estimated above (~5.0×10^3 pN μm^{-1}) is expressed as ~$5\bar{k}$; therefore we chose k_b ranging from 1 to 20 in the simulations. Other simulation parameters are expressed in units of a combination of $\bar{\xi}$, $\bar{v}$ and $\bar{k}$. For instance, the full expression of the inverse translational damping coefficient at its chosen value should be $\alpha_{||} = 10\,\bar{v}\,\bar{k}^{-1}\,\bar{\xi}^{-1}$.

Data analysis for bead–spring model simulations

All calculations and data analysis in active solid simulations followed the same procedures as described above for bacterial active solids, except that the local mass elements and the associated collective velocity field $\mathbf{v}(\mathbf{r}, t)$ obtained by optical flow analysis were now replaced by the active particles and their velocities. For modelled active solids under isotropic lateral confinement (that is, in circular geometry), we found that the oscillation amplitude of the radial component of spatially averaged velocity of active particles was also nearly zero (Extended Data Fig. 5e), which is similar to that in experiments (Fig. 1f). To obtain the phase diagram of global motion modes in modelled active solids under isotropic lateral confinement (Fig. 4a), 120 independent simulation runs were performed for each parameter set (v_0, k_b), and the mode of emergent global motion was determined for each simulation run at steady state. The mode that emerged in >50% of the 120 simulation runs was taken as the dominant mode of global motion at the parameter set (v_0, k_b), and the mean oscillation frequency at (v_0, k_b) was computed by averaging the frequencies of those simulation runs displaying the dominant mode.

Reporting summary

Further information on research design is available in the Nature Portfolio Reporting Summary linked to this article.

Data availability

The data supporting the findings of this study are included within the paper and its Supplementary Information. All other data that support the plots within this paper and other findings of this study are available from the corresponding author upon reasonable request.

Code availability

The custom codes used in this study are available from the corresponding author upon request.

References

44. Gibbs, K. A., Urbanowski, M. L. & Greenberg, E. P. Genetic determinants of self identity and social recognition in bacteria. *Science* **321**, 256–259 (2008).
45. Romero, D. & Kolter, R. Functional amyloids in bacteria. *Int. Microbiol.* **17**, 65–73 (2014).
46. Xu, H., Dauparas, J., Das, D., Lauga, E. & Wu, Y. Self-organization of swimmers drives long-range fluid transport in bacterial colonies. *Nat. Commun.* **10**, 1792 (2019).
47. Zuo, W. & Wu, Y. Dynamic motility selection drives population segregation in a bacterial swarm. *Proc. Natl Acad. Sci. USA* **117**, 4693–4700 (2020).
48. Roberts, M. E. & Stewart, P. S. Modeling antibiotic tolerance in biofilms by accounting for nutrient limitation. *Antimicrob. Agents Chemother.* **48**, 48–52 (2004).

Acknowledgements

We thank Y. Li and W. Zuo for building the image acquisition and microscope stage temperature-control systems, K. Gibbs (Harvard University) for providing the bacterial strains, S. Liu for helpful discussions, S. Liu for assistance in experiments and L. Xu (CUHK) for assistance with bulk rheology measurement. Y.H. and R.Z. thank Q. Wang and J. Tian for fruitful discussions. This work was supported by the Research Grants Council of Hong Kong SAR (RGC ref. no. RFS2021-4S04, 14303918, 14306820, to Y.W.; ref. no. 16300221, to R.Z.), the Ministry of Science and Technology Most China (2020YFA0910700, to Y.W.), and CUHK Direct Grants (to Y.W.).

Author contributions

H.X. discovered the phenomena, designed the study, performed experiments, performed simulations, and analysed and interpreted the data. Y.H. and R.Z. developed the theory and improved the simulations. Y.W. conceived the project, designed the study, and analysed and interpreted the data. R.Z. and Y.W. supervised the study. Y.W. wrote the first draft and all authors contributed to the revision of the manuscript.

Competing interests

The authors declare no competing interests.

Additional information

Extended data is available for this paper at https://doi.org/10.1038/s41567-022-01836-0.

Supplementary information The online version contains supplementary material available at https://doi.org/10.1038/s41567-022-01836-0.

Correspondence and requests for materials should be addressed to Yilin Wu.

Peer review information *Nature Physics* thanks Jing Yan, Thomas Angelini and Cristian Huepe for their contribution to the peer review of this work.

https://doi.org/10.1038/s41567-022-01836-0

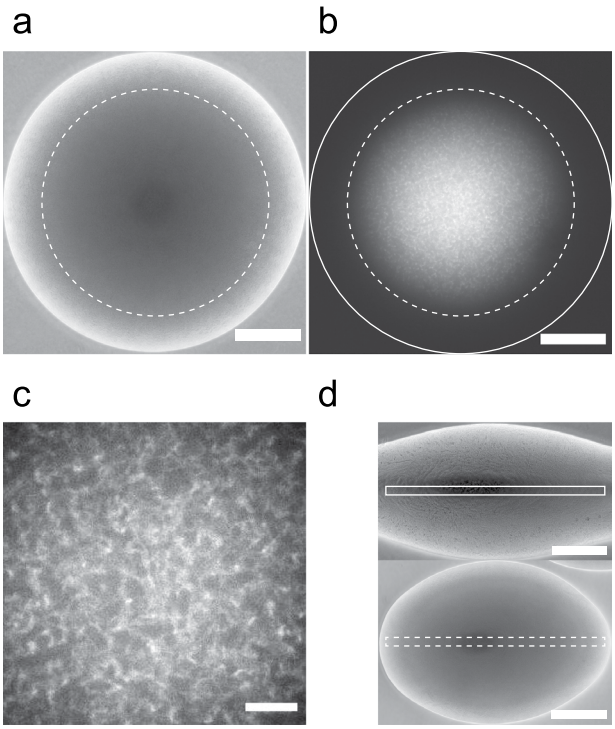

Extended Data Fig. 1 | *Proteus mirabilis* colonies at the early stage of biofilm development with prominent production of extracellular polymer matrix. (**a**) Phase-contrast image of a circular disk-shaped *P. mirabilis* colony grown for 14 hr at 37 °C after inoculation with overnight culture (Methods). Scale bar, 500 μm. (**b**) Fluorescent image of extracellular amyloid fibrils matrix labelled by Thioflavin T (Methods) in the *P. mirabilis* biofilm shown in panel a. The outer rim of *P. mirabilis* colonies at this development stage is mostly occupied by immotile cells that have transitioned to the sessile state but expressed little extracellular matrix. The width of this outer immotile rim varies from tens to hundreds of μm across different colonies; in the case of panel a, the immotile rim ranges from radius R = ~860 μm (measured from the colony centre) to R = 1154 μm (i.e, the colony edge), spanning a width of ~300 μm. The inner region of the colonies with Thioflavin T fluorescence (that is, the biofilm region; enclosed by the dashed circle in panels a,b) is where we choose to study and refer to as early-stage biofilm or bacterial active solid, such as the fields in main text Figs. 1c,d and 3a. The immotile outer rim of the colony serves as the lateral spatial confinement for the bacterial active solid. Scale bar, 500 μm. (**c**) Enlarged view of the centre of panel b. Scale bar, 100 μm. (d) Phase-contrast images of oval-shaped *P. mirabilis* colonies with various values of the eccentricity. Scale bars, 500 μm. The field in main text Fig. 2a corresponds to the stripe region enclosed by the dashed rectangle in panel d.

https://doi.org/10.1038/s41567-022-01836-0

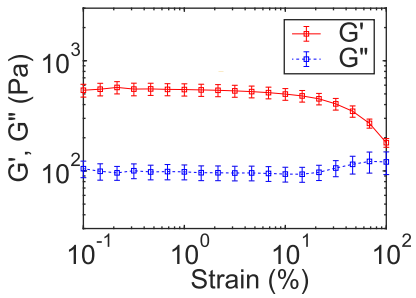

Extended Data Fig. 2 | Dynamic moduli of the bacterial active solid derived from early-stage *P. mirabilis* biofilms. Storage (G′; red) and loss (G″; blue) shear modulus of the bacterial active solid as a function of strain were measured by bulk rheometry with a cone-plate rheometer in shear-strain-amplitude sweep mode (at constant frequency) (Methods). The oscillation frequency and the temperature of the rheometer were set at 1 Hz and 37 °C, respectively. Data are presented as mean + /-S.D. (N = 3). The solid and dashed lines are guides to the eye.

https://doi.org/10.1038/s41567-022-01836-0

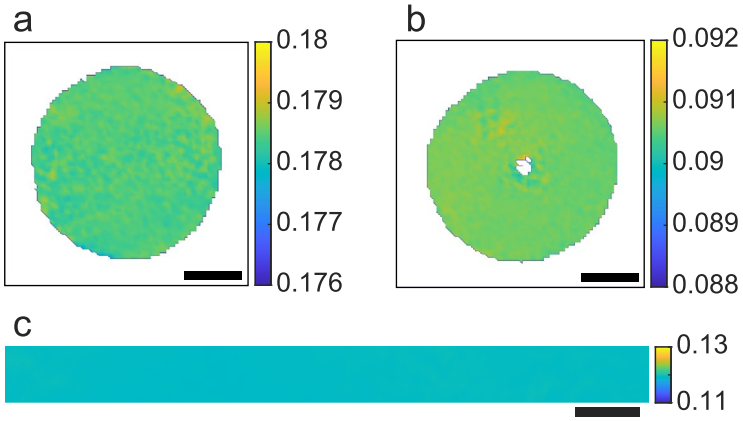

Extended Data Fig. 3 | Spatial distribution of local oscillation frequency in bacterial active solids. Panels a and b shows the frequency distribution in circular disk-shaped bacterial active solids undergoing global oscillatory translation and oscillatory rotation, respectively, with the colour bars indicating the magnitude of local oscillation frequency (unit: Hz). Scale bars, 500 μm. The frequency at the centre of panel b is absent because the velocity there is vanishing. Panel c shows the frequency distribution in a rectangular region of an oval-shaped bacterial active solid that displays the transverse standing wave, with the colour bar indicating the magnitude of local oscillation frequency (unit: Hz). The longer side of the selected region is parallel to the major axis of symmetry of the bacterial active solid. Scale bar, 200 μm.

https://doi.org/10.1038/s41567-022-01836-0

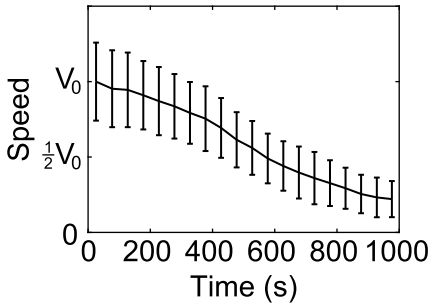

Extended Data Fig. 4 | Tuning single-cell speed of *P. mirabilis* via violet-light illumination. To obtain this plot, cells were extracted from the *P. mirabilis*-based bacterial active solids that were undergoing either global oscillatory translation or global oscillatory rotation; the extracted cells were mixed with 0.02% Tween 20 and deposited on 0.6% LB agar surface, forming a quasi-2D dilute bacterial suspension drop. *P. mirabilis* cells in the prepared quasi-2D dilute bacterial suspension drop were continuously illuminated by 406 nm violet light starting from T = 0 s while being tracked in phase-contrast microscopy (Methods); note that for single-cell tracking, a 20x objective lens was used. The speed of an individual cell at a specific time T was computed based on its trajectory tracked from (T-0.5) s to (T + 0.5) s; the single-cell speeds computed from (T-25) s to (T + 25) s were then averaged and taken to be the mean cell speed at T. Data shown in the plot was normalized by the mean speed at T = 0 s (that is, the free-swimming speed of cells without blue light illumination; $V_0 = 26.7 \pm 6.9$ μm/s; mean±S.D., N = 2500). Data are presented as mean + /-S.D. (N = 2500).

https://doi.org/10.1038/s41567-022-01836-0

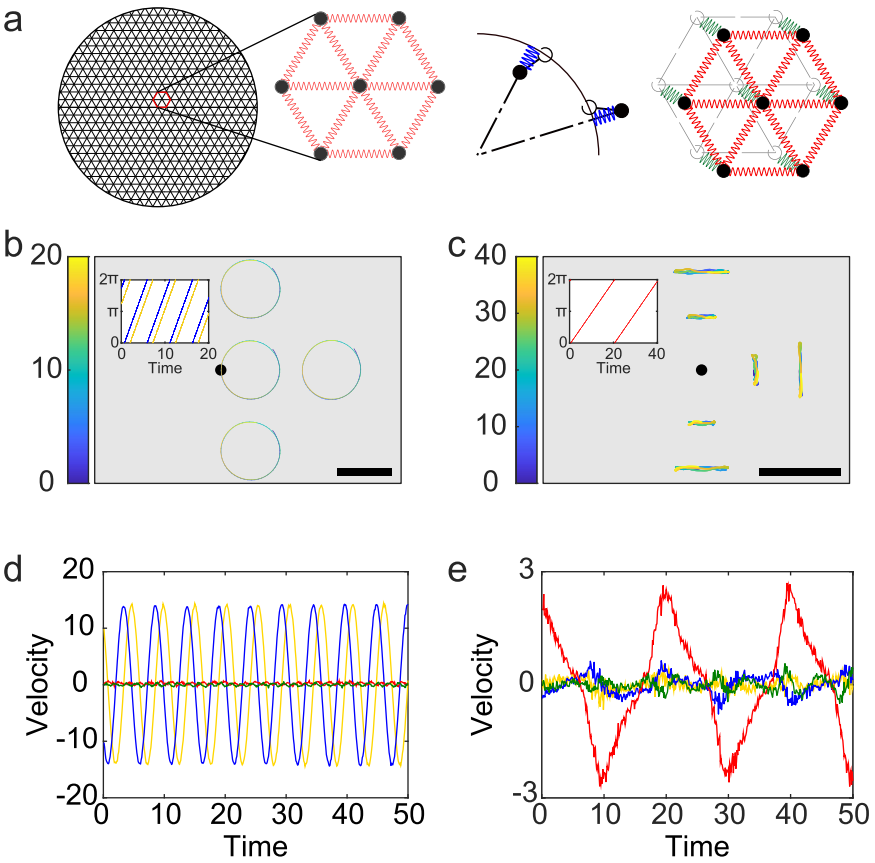

Extended Data Fig. 5 | Emergent global motion modes in modelled active solid under isotropic lateral confinement. (a) Schematic diagram of the bead–spring model for active solid under two-dimensional isotropic lateral confinement (Methods). The model consists of $N = 511$ self-propelled particles (black solid circles). Every nearest-neighbour pair of particles is connected by an interparticle spring with spring constant k_b (red). The particles also experience elastic forces due to substrate adhesion and lateral spatial confinement (see main text) via a restoring spring (green) and a boundary spring (blue) with spring constant k_s and k_r, respectively. The three spring constants together determine the system's local elasticity. In simulations the interparticle spring constant k_b was used as a proxy for the system's local elasticity, with the ratios between k_b, k_s and k_r fixed. (**b**,**c**) Representative trajectories of particles in the modelled active solid that underwent global oscillatory translation (panel b) and oscillatory rotation (panel c). Most particles (except those very near the centre or the boundary) followed periodically oscillating quasi-circular trajectories (at relatively high activity; panel b; Supplementary Video 9) or quasi-linear concentric trajectories (at relatively low activity; panel c; Supplementary Video 10) with highly synchronized phases (insets of panel b,c), in the same manner as the motion of matrix-embedded cells in the experiments undergoing global oscillatory translation (main text Fig. 1a) or rotation (main text Fig. 1b), respectively. Black dot in each panel indicates the centre of the simulation domain. Scale bars represent 1/3 of the interparticle distance at equilibrium and colour map indicates time. Insets: Oscillation phases of individual particle's velocity components plotted in the same way as in insets of Fig. 1a,b. Simulation parameters: $v_0 = 15$ (panel b) or $v_0 = 3$ (panel c), $k_b = 12$, $k_r = 0.6$, and $k_s = 0.044$. (**d**,**e**) Temporal dynamics of spatially averaged particle velocity in the modelled active solid in global oscillatory translation mode (panel d) or oscillatory rotation mode (panel e). The velocity was averaged over all particles in the simulation and then decomposed as Cartesian (yellow and blue traces) and polar-coordinate components (red: tangential or azimuthal component; green: radial component). The spatially averaged particle velocity in the two emergent modes was characterized by distinct temporal dynamics in Cartesian or polar coordinates similar to that found in the experiments (main text Fig. 1e,f). Simulation parameters are identical to those used in panels b,c.

https://doi.org/10.1038/s41567-022-01836-0

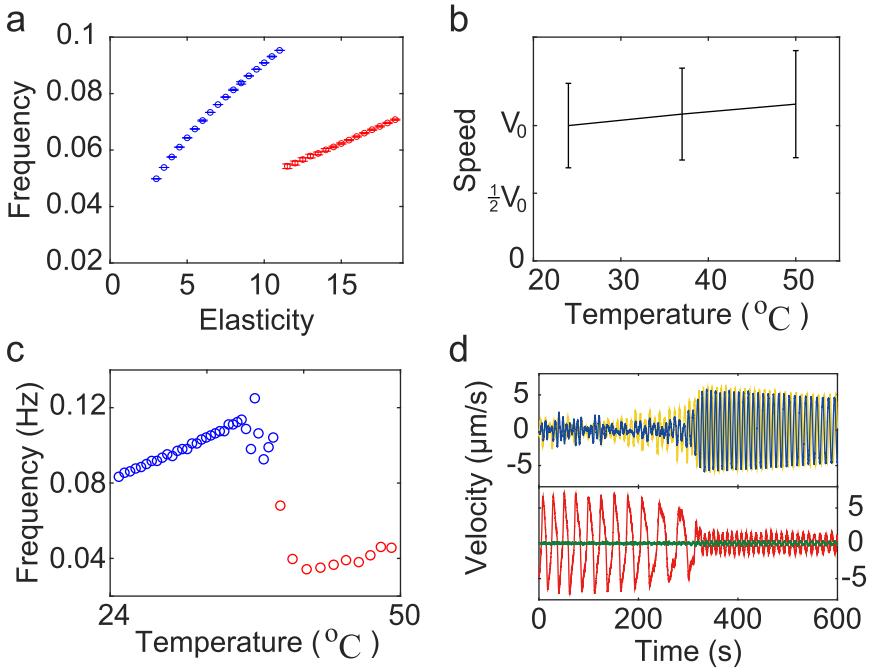

Extended Data Fig. 6 | Elasticity dependence of the global motion modes in active solids under isotropic lateral confinement. (**a**) Oscillation frequency of global motion modes in modelled active solids as a function of k_b (fixing v_0 = 4). Colour of data points indicates the mode of global motion (blue: oscillatory translation; red: oscillatory rotation). Data are presented as mean + /-S.D. (N=100 simulation runs). **(b)** Temperature dependence of *P. mirabilis* single-cell speed. *P. mirabilis* cells in quasi-2D dilute bacterial suspension drops (prepared in the same manner as described in the caption of Extended Data Fig. 4) were tracked in fluorescent microscopy while the environmental temperature was varied from 24 °C to 50 °C with a custom-built temperature-control system (Methods). As shown in the plot the speed of cells only changed slightly in this temperature range (up to ~15%). The mean speed of cells at a specific temperature was computed based on 1-s segments of cell trajectories tracked in a 200-s time window. Data shown in the plot was normalized by the mean speed at temperature 24 °C. Data are presented as mean + /-S.D. (N = 2500). (**c**,**d**) Transition of global motion modes in bacterial active solids controlled by temperature. Panel c shows the temperature dependence of oscillation frequency in the bacterial active solid during mode transition. Colour of data points indicates the mode of global motion (blue: oscillatory translation; red: oscillatory rotation). Panel d shows the temporal dynamics of spatially averaged collective velocity during transition from the oscillatory rotation mode to the oscillatory translation mode following the decrease of temperature. The spatially averaged collective velocity was decomposed as Cartesian components (yellow and blue traces; upper part of panel d) and polar-coordinate components (red: tangential or azimuthal component, green: radial component; lower part of panel d). Data in panels c,d were from a representative experiment (>5 replicates).

https://doi.org/10.1038/s41567-022-01836-0

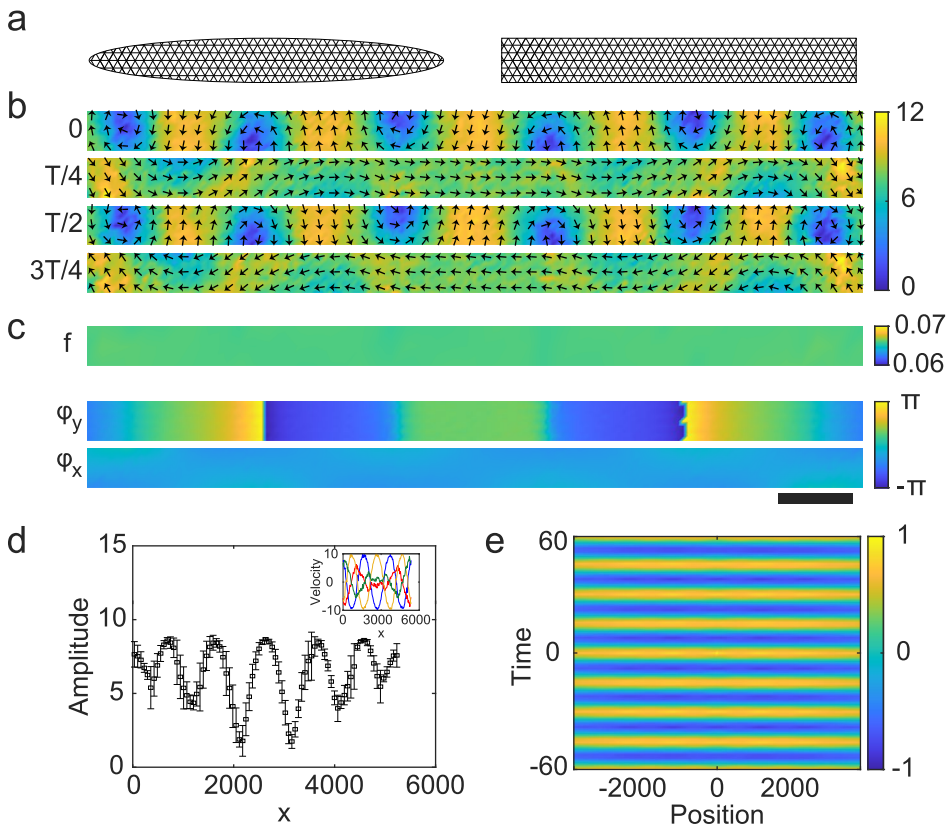

Extended Data Fig. 7 | Self-sustained transverse standing waves in modelled active solids under anisotropic lateral confinement. This figure is associated with main text Fig. 4d. Simulation parameters: $v_0 = 10$, $k_b = 4$, $k_r = 0.2$, and $k_s = 0.015$. **(a)** Schematic diagrams of the bead–spring model for active solid under two-dimensional anisotropic lateral confinement (Methods). The elliptical confinement (left) mimics the anisotropic lateral confinement geometry of oval-shaped bacterial active solids used in main text Fig. 2. Rectangular lateral confinement (right) produces similar simulation results. (**b**) Time sequence of particle velocity field in a modelled active solid under elliptical lateral confinement that displays the transverse standing wave. The longer side of the rectangular domain shown here is in parallel to the major axis of the elliptical confinement. T denotes the period of oscillation. Arrows represent velocity direction and colour map indicates velocity magnitude. (**c**) Spatial distributions of local oscillation frequency and phase associated with panel b. The local oscillation frequency is homogeneous in space (upper part of the panel, with the colour bar indicating the magnitude of frequency). The phase of parallel (v_x; parallel to the major axis) and transverse (v_y; perpendicular to the major axis) component of particle velocity is denoted as φ_x (lower) and φ_y (upper), respectively. Scale bar under panel c is shared by panel b and represents 7.7 times of the interparticle distance at equilibrium. (**d**) Averaged amplitude distribution of v_y along major axis of the modelled active solid. Data are presented as mean + /-S.D. (N=100 simulation runs). Inset: temporal evolution of v_y profile in panel b along the major axis of the modelled active solid, with colours representing time (blue: 0; red: T/4; yellow: T/2; green: 3 T/4). (**e**) Spatiotemporal autocorrelation of v_x along the major axis of the modelled active solid (that is, the abscissa of the figure); the pattern of periodic, horizontal lanes with high correlation is similar to that seen in experiment (main text Fig. 2e). Colour map at right side indicates the autocorrelation magnitude (a.u.).

https://doi.org/10.1038/s41567-022-01836-0

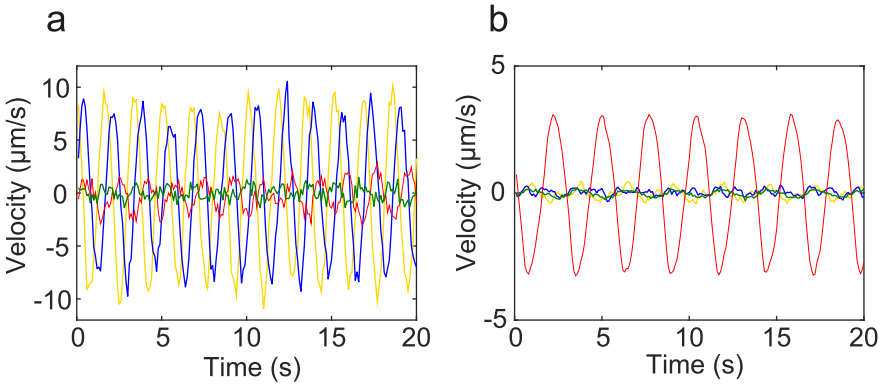

Extended Data Fig. 8 | Emergent global motion modes in bacterial active solids derived from *S. marcescens* biofilms. Temporal dynamics of spatially averaged collective velocity in the global oscillatory translation mode (panel a) and oscillatory rotation mode (panel b). The spatially averaged collective velocity was decomposed as Cartesian (yellow and blue traces) and polar-coordinate components (red: tangential or azimuthal component; green: radial component). In the oscillatory translation mode, the polar-coordinate components are negligible; in the oscillatory rotation mode, both the radial and the Cartesian components are negligible.

https://doi.org/10.1038/s41567-022-01836-0

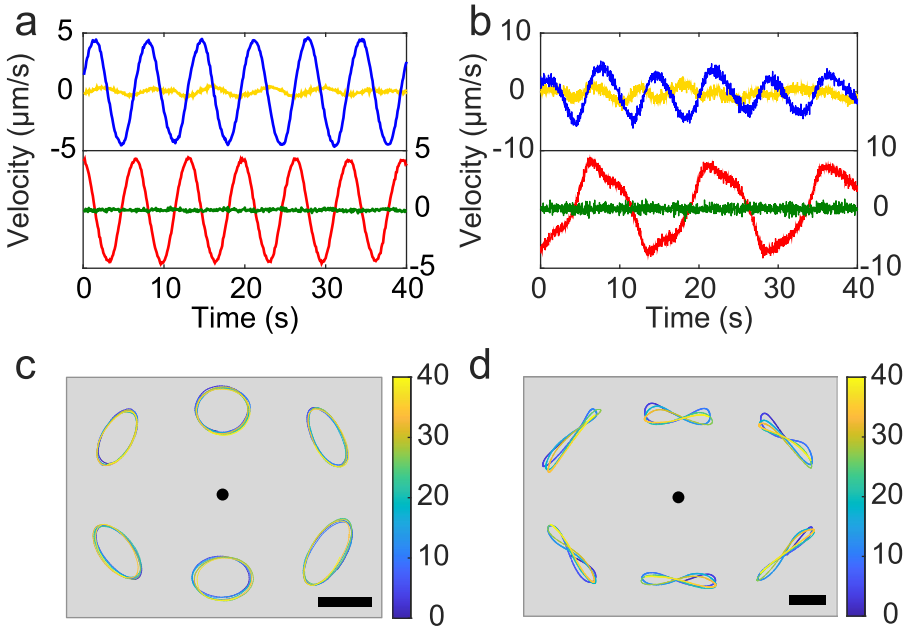

Extended Data Fig. 9 | Coexistence of two global motion modes in bacterial active solids under isotropic lateral confinement. (**a**,**b**) Temporal dynamics of spatially averaged collective velocity in circular disk-shaped bacterial active solids where the oscillatory translation and oscillatory rotation modes co-existed with identical frequencies ($f_t = f_r = 0.15$ Hz; panel a) or with the frequency of the oscillatory translation mode doubled ($f_t = 0.14$ Hz, $f_r = 0.07$ Hz; panel b). The velocity was decomposed as Cartesian (yellow and blue traces) and polar-coordinate components (red: tangential component; green: radial component). (**c**,**d**) Panels c and d display representative trajectories of mass elements in bacterial active solids analysed in panels a and b, respectively. In each panel the trajectories were obtained by integrating the spatially averaged collective velocity over a $50\,\mu m \times 50\,\mu m$ domain located ~500 μm from the centre of the disk-shaped bacterial active solid (black dot) at different polar angles. The trajectories were brought close to the centre for better visualization, and thus the scale bars (panel c, $10\,\mu m$; panel d, $20\,\mu m$) apply to the trajectories only. Colour map indicates time (unit: s).

https://doi.org/10.1038/s41567-022-01836-0

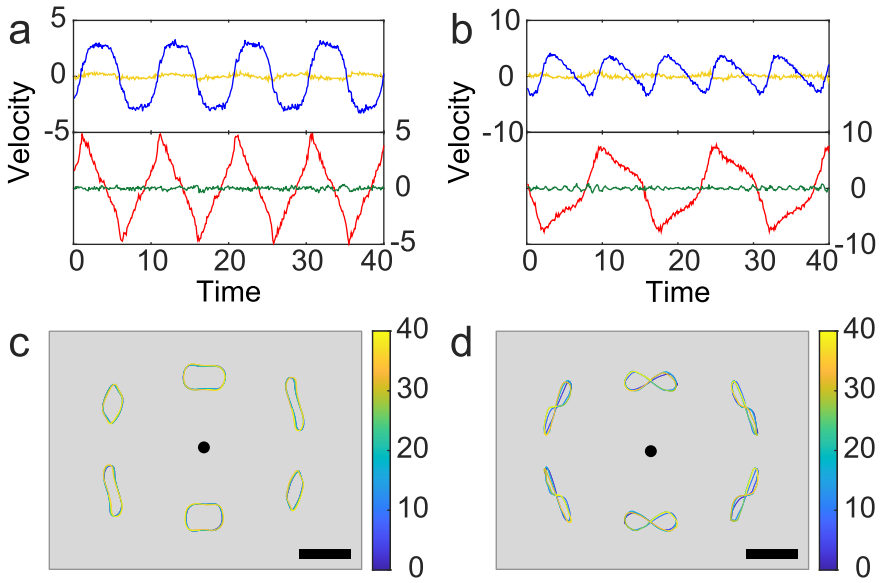

Extended Data Fig. 10 | Coexistence of two global motion modes in modelled active solid under isotropic lateral confinement. (**a**,**b**) Temporal dynamics of collective velocity of the system where oscillatory translation and oscillatory rotation modes co-existed with identical frequencies ($f_t = f_r = 0.10$; panel a) or with the frequency of the oscillatory translation mode doubled ($f_t = 0.13$, $f_r = 0.07$; panel b). The collective velocity was averaged over all particles in the simulation and then decomposed as Cartesian (yellow and blue traces; upper part of each panel) and polar-coordinate components (red: tangential or azimuthal component, green: radial component; lower part of each panel). Simulation parameters: panel a, $v_0 = 5$, $k_b = 12$; panel b, $v_0 = 9$, $k_b = 16$; the ratios between k_b, k_s and k_r are fixed (Methods). (**c**,**d**) Panels c and d display the trajectory of representative particles in the simulations analysed in panels a and b, respectively. In each panel the particle was chosen at ~5 times of the equilibrium interparticle distance from the centre of the circular simulation domain (black dot) at different polar angles. The trajectories were brought close to the centre for better visualization, and thus the scale bars (indicating 1/3 interparticle distance at equilibrium) apply to the trajectories only. Colour map indicates time.

nature portfolio

Corresponding author(s): Yilin Wu

Last updated by author(s): Oct 11, 2022

Reporting Summary

Nature Portfolio wishes to improve the reproducibility of the work that we publish. This form provides structure for consistency and transparency in reporting. For further information on Nature Portfolio policies, see our Editorial Policies and the Editorial Policy Checklist.

Statistics

For all statistical analyses, confirm that the following items are present in the figure legend, table legend, main text, or Methods section.

n/a	Confirmed
☐	☒ The exact sample size (*n*) for each experimental group/condition, given as a discrete number and unit of measurement
☐	☒ A statement on whether measurements were taken from distinct samples or whether the same sample was measured repeatedly
☒	☐ The statistical test(s) used AND whether they are one- or two-sided *Only common tests should be described solely by name; describe more complex techniques in the Methods section.*
☒	☐ A description of all covariates tested
☒	☐ A description of any assumptions or corrections, such as tests of normality and adjustment for multiple comparisons
☒	☐ A full description of the statistical parameters including central tendency (e.g. means) or other basic estimates (e.g. regression coefficient) AND variation (e.g. standard deviation) or associated estimates of uncertainty (e.g. confidence intervals)
☒	☐ For null hypothesis testing, the test statistic (e.g. *F*, *t*, *r*) with confidence intervals, effect sizes, degrees of freedom and *P* value noted *Give P values as exact values whenever suitable.*
☒	☐ For Bayesian analysis, information on the choice of priors and Markov chain Monte Carlo settings
☒	☐ For hierarchical and complex designs, identification of the appropriate level for tests and full reporting of outcomes
☒	☐ Estimates of effect sizes (e.g. Cohen's *d*, Pearson's *r*), indicating how they were calculated

Our web collection on statistics for biologists contains articles on many of the points above.

Software and code

Policy information about availability of computer code

Data collection	The following software was used for data collection: NIS Elements (Nikon)
Data analysis	The following softwares were used for data analysis: The open-source Fiji (ImageJ) software (http://fiji.sc/Fiji); MATLAB (The MathWorks, Inc.).

For manuscripts utilizing custom algorithms or software that are central to the research but not yet described in published literature, software must be made available to editors and reviewers. We strongly encourage code deposition in a community repository (e.g. GitHub). See the Nature Portfolio guidelines for submitting code & software for further information.

Data

Policy information about availability of data

All manuscripts must include a data availability statement. This statement should provide the following information, where applicable:

- Accession codes, unique identifiers, or web links for publicly available datasets
- A description of any restrictions on data availability
- For clinical datasets or third party data, please ensure that the statement adheres to our policy

The data supporting the findings of this study are included within the paper and its Supplementary Materials. Source data are available for this paper. All other data that support the plots within this paper and other findings of this study are available from the corresponding author upon reasonable request.

Human research participants

Policy information about studies involving human research participants and Sex and Gender in Research.

Reporting on sex and gender	*Use the terms sex (biological attribute) and gender (shaped by social and cultural circumstances) carefully in order to avoid confusing both terms. Indicate if findings apply to only one sex or gender; describe whether sex and gender were considered in study design whether sex and/or gender was determined based on self-reporting or assigned and methods used. Provide in the source data disaggregated sex and gender data where this information has been collected, and consent has been obtained for sharing of individual-level data; provide overall numbers in this Reporting Summary. Please state if this information has not been collected. Report sex- and gender-based analyses where performed, justify reasons for lack of sex- and gender-based analysis.*
Population characteristics	*Describe the covariate-relevant population characteristics of the human research participants (e.g. age, genotypic information, past and current diagnosis and treatment categories). If you filled out the behavioural & social sciences study design questions and have nothing to add here, write "See above."*
Recruitment	*Describe how participants were recruited. Outline any potential self-selection bias or other biases that may be present and how these are likely to impact results.*
Ethics oversight	*Identify the organization(s) that approved the study protocol.*

Note that full information on the approval of the study protocol must also be provided in the manuscript.

Field-specific reporting

Please select the one below that is the best fit for your research. If you are not sure, read the appropriate sections before making your selection.

☐ Life sciences ☐ Behavioural & social sciences ☐ Ecological, evolutionary & environmental sciences

For a reference copy of the document with all sections, see nature.com/documents/nr-reporting-summary-flat.pdf

Life sciences study design

All studies must disclose on these points even when the disclosure is negative.

Sample size	*Describe how sample size was determined, detailing any statistical methods used to predetermine sample size OR if no sample-size calculation was performed, describe how sample sizes were chosen and provide a rationale for why these sample sizes are sufficient.*
Data exclusions	*Describe any data exclusions. If no data were excluded from the analyses, state so OR if data were excluded, describe the exclusions and the rationale behind them, indicating whether exclusion criteria were pre-established.*
Replication	*Describe the measures taken to verify the reproducibility of the experimental findings. If all attempts at replication were successful, confirm this OR if there are any findings that were not replicated or cannot be reproduced, note this and describe why.*
Randomization	*Describe how samples/organisms/participants were allocated into experimental groups. If allocation was not random, describe how covariates were controlled OR if this is not relevant to your study, explain why.*
Blinding	*Describe whether the investigators were blinded to group allocation during data collection and/or analysis. If blinding was not possible, describe why OR explain why blinding was not relevant to your study.*

Behavioural & social sciences study design

All studies must disclose on these points even when the disclosure is negative.

Study description	*Briefly describe the study type including whether data are quantitative, qualitative, or mixed-methods (e.g. qualitative cross-sectional, quantitative experimental, mixed-methods case study).*
Research sample	*State the research sample (e.g. Harvard university undergraduates, villagers in rural India) and provide relevant demographic information (e.g. age, sex) and indicate whether the sample is representative. Provide a rationale for the study sample chosen. For studies involving existing datasets, please describe the dataset and source.*
Sampling strategy	*Describe the sampling procedure (e.g. random, snowball, stratified, convenience). Describe the statistical methods that were used to predetermine sample size OR if no sample-size calculation was performed, describe how sample sizes were chosen and provide a rationale for why these sample sizes are sufficient. For qualitative data, please indicate whether data saturation was considered, and what criteria were used to decide that no further sampling was needed.*

Data collection	*Provide details about the data collection procedure, including the instruments or devices used to record the data (e.g. pen and paper, computer, eye tracker, video or audio equipment) whether anyone was present besides the participant(s) and the researcher, and whether the researcher was blind to experimental condition and/or the study hypothesis during data collection.*
Timing	*Indicate the start and stop dates of data collection. If there is a gap between collection periods, state the dates for each sample cohort.*
Data exclusions	*If no data were excluded from the analyses, state so OR if data were excluded, provide the exact number of exclusions and the rationale behind them, indicating whether exclusion criteria were pre-established.*
Non-participation	*State how many participants dropped out/declined participation and the reason(s) given OR provide response rate OR state that no participants dropped out/declined participation.*
Randomization	*If participants were not allocated into experimental groups, state so OR describe how participants were allocated to groups, and if allocation was not random, describe how covariates were controlled.*

Ecological, evolutionary & environmental sciences study design

All studies must disclose on these points even when the disclosure is negative.

Study description	*Briefly describe the study. For quantitative data include treatment factors and interactions, design structure (e.g. factorial, nested, hierarchical), nature and number of experimental units and replicates.*
Research sample	*Describe the research sample (e.g. a group of tagged Passer domesticus, all Stenocereus thurberi within Organ Pipe Cactus National Monument), and provide a rationale for the sample choice. When relevant, describe the organism taxa, source, sex, age range and any manipulations. State what population the sample is meant to represent when applicable. For studies involving existing datasets, describe the data and its source.*
Sampling strategy	*Note the sampling procedure. Describe the statistical methods that were used to predetermine sample size OR if no sample-size calculation was performed, describe how sample sizes were chosen and provide a rationale for why these sample sizes are sufficient.*
Data collection	*Describe the data collection procedure, including who recorded the data and how.*
Timing and spatial scale	*Indicate the start and stop dates of data collection, noting the frequency and periodicity of sampling and providing a rationale for these choices. If there is a gap between collection periods, state the dates for each sample cohort. Specify the spatial scale from which the data are taken*
Data exclusions	*If no data were excluded from the analyses, state so OR if data were excluded, describe the exclusions and the rationale behind them, indicating whether exclusion criteria were pre-established.*
Reproducibility	*Describe the measures taken to verify the reproducibility of experimental findings. For each experiment, note whether any attempts to repeat the experiment failed OR state that all attempts to repeat the experiment were successful.*
Randomization	*Describe how samples/organisms/participants were allocated into groups. If allocation was not random, describe how covariates were controlled. If this is not relevant to your study, explain why.*
Blinding	*Describe the extent of blinding used during data acquisition and analysis. If blinding was not possible, describe why OR explain why blinding was not relevant to your study.*

Did the study involve field work? ☐ Yes ☒ No

Reporting for specific materials, systems and methods

We require information from authors about some types of materials, experimental systems and methods used in many studies. Here, indicate whether each material, system or method listed is relevant to your study. If you are not sure if a list item applies to your research, read the appropriate section before selecting a response.

Materials & experimental systems

n/a	Involved in the study
☒	☐ Antibodies
☒	☐ Eukaryotic cell lines
☒	☐ Palaeontology and archaeology
☒	☐ Animals and other organisms
☒	☐ Clinical data
☒	☐ Dual use research of concern

Methods

n/a	Involved in the study
☒	☐ ChIP-seq
☒	☐ Flow cytometry
☒	☐ MRI-based neuroimaging